NASA CR-1469

NASA CONTRACTOR
REPORT

NASA CR-14

TECH LIBRARY KAFB, NM

STUDY OF RADIATION HAZARDS TO MAN ON EXTENDED NEAR EARTH MISSIONS

by S. B. Curtis, W. R. Doherty, and M. C. Wilkinson

Prepared by
THE BOEING COMPANY
Seattle, Wash.
for

NATIONAL AERONAUTICS AND SPACE ADMINISTRATION • WASHINGTON, D. C. • DECEMBER 1969

NASA CR-1469

STUDY OF RADIATION HAZARDS TO MAN

ON EXTENDED NEAR EARTH MISSIONS

By S. B. Curtis,* W. R. Doherty, and
M. C. Wilkinson

*Consultant, Lawrence Radiation Laboratory

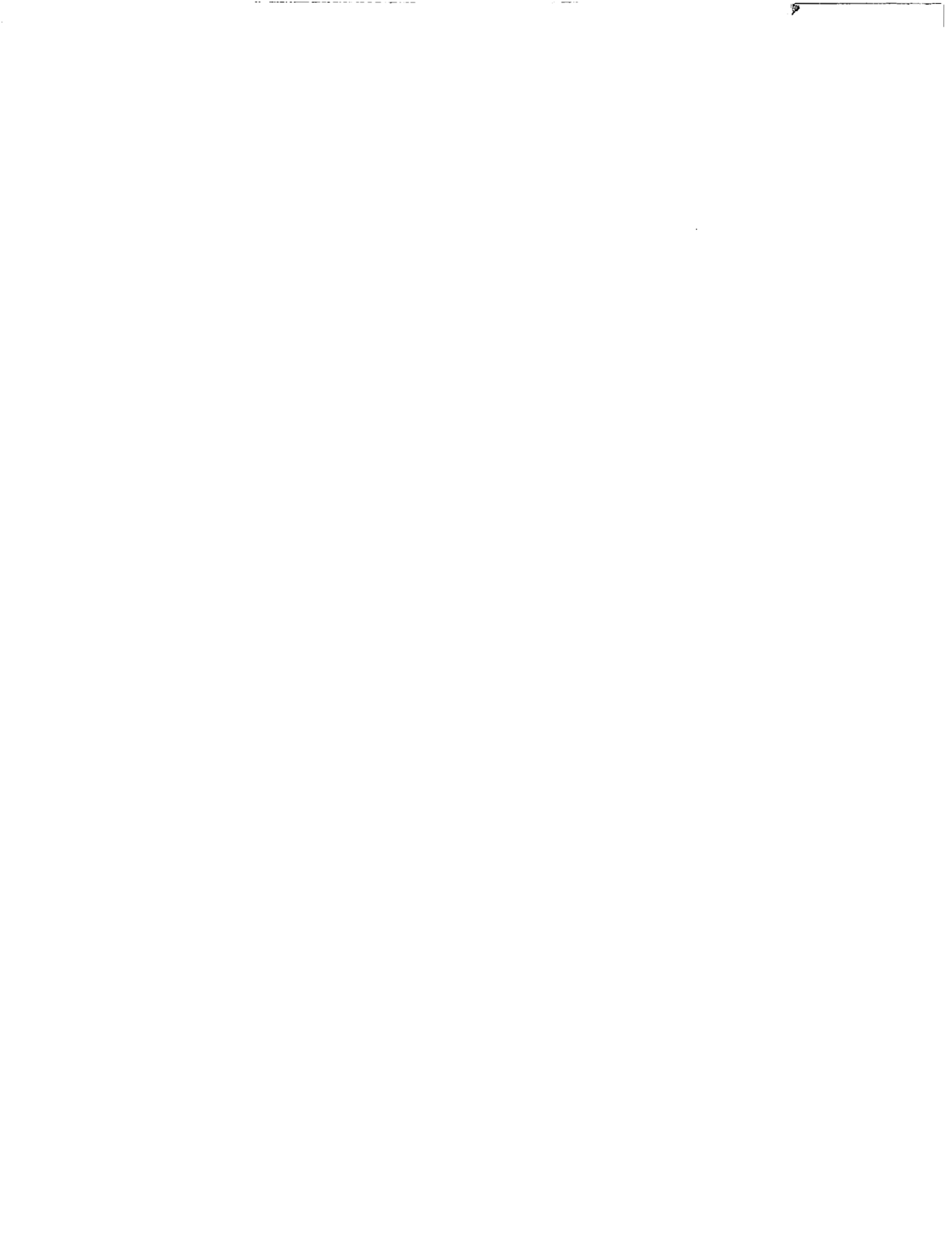Issued by Originator as Report No. D2-114299-1

FOREWORD

This report is submitted to the National Aeronautics and Space Administration, Headquarters Branch, Washington, D.C., in accordance with the requirements set forth in NASA contract NASw-1362. The work herein reported was performed by W. R. Doherty and M. C. Wilkinson of the Space Physics Group, Aerospace Systems Division, The Boeing Company, and by Dr. Stanley B. Curtis of the Lawrence Radiation Laboratory, consultant to The Boeing Company. This work was done under the supervision of Dr. L. G. Despain.

ABSTRACT

This study identifies the particle types and energies which are impor-
tant in the evaluation of the radiation hazard on long manned missions
inside the earth's magnetosphere. Spectra of the trapped protons and
electrons encountered at synchronous altitude and in a 260 nautical mile,
50^0 inclination circular orbit are presented, along with estimates of
the uncertainties. These spectra have been used to determine depth-dose
curves behind typical aluminum shielding. Recent high energy data from
Oak Ridge National Laboratory were used to evaluate the importance of
the high energy (400 MeV to 2000 MeV) protons in the Galactic and Solar
Cosmic-ray spectra in producing dose. The secondary dose components from
300 MeV/nucleon neon ions in water were estimated using cosmic-ray emul-
sion data.

CONTENTS

LIST OF FIGURES

INTRODUCTION

In the first part of this study (1) a summary of the radiation environ-
ment beyond the earth's magnetosphere was made from the data available
in early 1967. The interaction of the environment with aluminum
shielding was considered, and the available knowledge of biological
effects was used to evaluate the relative importance of the energies and
types of particles encountered in the deep space environment.

In this study we extend the environment description to include the
earth's magnetosphere. Two earth orbital missions, near earth (260
nautical miles circular) and at synchronous altitude, are examined in
detail. Geomagnetic cutoff effects are also considered. This environ-
ment is then analyzed to determine the important particle energies in
evaluating biological effects. In addition, the proton shielding cal-
culations previously presented are extended in scope by using recent
data from Oak Ridge National Laboratory to treat the high energy protons
(400 to 2000 MeV). A method for determining the dose resulting from the
high energy heavy particles encountered in the galactic cosmic rays is
also developed.

EARTH ORBITAL STUDIES

RADIATION ENVIRONMENT DEFINITION

Earth orbital missions will encounter the environments discussed in (1);
the Galactic Cosmic Rays (GCR), Solar Cosmic Rays (SCR), and Energetic
Storm Particles (ESP). However, the spectra of these environments will
be modified by the geomagnetic field. In addition, these missions en-
counter the charged particles trapped in the geomagnetic field. This
includes the natural Van Allen Belts and the remnants of the relativistic
electron belts artificially produced by high altitude nuclear tests.
The only identifiable artificial belt remaining is the "Starfish" belt
produced by a high altitude burst over Johnson Island on July 9, 1962,
and its fluxes are significant only near the heart of the inner zone.
Excellent reviews (2, 3, 4) and a series of models (5, 6, 7) of the
trapped radiation belts have appeared. A complete description of the
trapped environment is beyond the scope of this study. A few remarks,
however, are pertinent.

It has been known for some time (8) that the flux of protons of energies
greater than 100 MeV exceeds 10^3 $cm^{-2}sec^{-1}$ in the heart of the inner
zone. This flux gives doses in excess of 10^4 rad/year behind $10g/cm^2$ of
aluminum. Hence, extended manned missions will avoid the intense regions
of the trapped belts until it is practical to provide extensive radiation
shielding. Early extended missions will encounter only the edges of the
Van Allen belt where the flux is characterized by strong variations; either
temporal or spatial and directional. The trapped belts are principally

composed of protons and electrons. The two basic natural sources of these belts are the galactic cosmic rays and the solar particles. As Stormer has shown, the primary particles themselves cannot be trapped unless they are scattered out of their phase-space trajectories, which connect with extra-magnetospheric space. Elastic scattering can be dis-counted as a source immediately for, if significant, this scattering will also contribute significantly to the loss from the trapping region. Of the inelastic events, the neutron albedo from the cosmic rays and the accelerative diffusion of the solar wind and storm particles are the most promising sources. The spectra and fluxes of trapped protons are in reasonable agreement with these source predictions, but there is con-siderable evidence that additional sources or redistributions are present (2). The distribution of protons is much more stable than the distribu-tion of electrons. This may not be surprising since we are comparing par-ticles with vastly different rigidities.

The trapped particle distributions are normally presented in the geo-magnetic B-L coordinates of McIlwain (9). The shell parameter, L, labels the dipole-like shell upon which the particles are trapped and B repre-sents the magnetic flux density at which the particles are locally mirroring. When losses or redistributions of the particles during a drift period are negligible, the flux and spectra are the same for all points having the same B and L. Consequently the B-L coordinate system is better suited for protons than for electrons. In fact, in the intense region of the inner belt where the losses are smallest, the most significant variation of the protons during a drift period is expected to be the non-uniform drift

3

velocity (10). Another practical variation or contribution to scatter in the data is the inadequacy of the magnetic field model employed to determine accurately the mirror point traces of the particles (11). This source of scatter is more important at low altitudes where the gradients of the distribution in B and L are greatest. Since the magnetic field at low altitudes has a slowly varying temporal component, this variation contributes to the time dependence of the low altitude proton fluxes. Another source of scatter in the proton data exists for directional detectors because of the anisotropic distribution of trapped particles. This is particularly true at low altitudes where the pitch-angle distributions are strongly dependent upon position and also where the east-west asymmetry in the energetic proton flux is greatest. Although the cyclic temporal variations may be averaged out in extended missions, we see that the most likely missions are left with a radiation environment which is more complex than that which would be experienced in the intense regions. In this study we shall exemplify these missions with a synchronous (geostationary) mission and a low altitude mission of intermediate inclination angle.

Synchronous Altitude Missions

The penetrating radiation at synchronous altitude is composed of the trapped electrons and the extramagnetospheric environment (solar particles and galactic cosmic-rays) as modified by the geomagnetic field. The trapped protons have a mean energy of 100 keV and thus interact only with the material which is within a few microns of the surface of the spacecraft.

The energetic electron fluxes at synchronous altitude are characterized by violent time variations as are most of the outer zone electron fluxes. Vette (6) has derived a composite model (AE3) of the electrons at L = 6.6 earth radii. The shell parameter, L, given by the Jensen and Cain field model (12) for a geostationary satellite lies between 6.59 and 6.98 earth radii, depending upon longitude. The mean flux has a strong local time dependence. However, an extended mission will see the environment averaged over local time. Figure 1 presents the extremes of the local time variation of the AE3 environment as well as the average over local time. This model environment is the best available at the present time.

Vette points out that the assumption of a normal distribution for the logarithm of the flux results in a reasonable fit to the available data. That is, the model probability density p(J) for the integral flux J (> E) is given by,

$$P(J) = \frac{1}{\sqrt{2\pi}\,\sigma} \frac{\log e}{J} \exp\left[-(\log J - \mu)^2/2\sigma^2\right], \quad \mu = <\log J>$$

where $\sigma = 0.62\, E^{0.2}$ increases with energy. The average flux <J> becomes

$$<J> = 10^{\left(\mu + \sigma^2/2\log e\right)}$$

We see that log <J> exceeds the <log J> = μ by a factor increasing with energy. For example, since AE3 gives $<J(> 1\ \text{MeV})> = 4.66 \times 10^5\ \text{cm}^{-2}\text{sec}^{-1}$, one obtains μ (1 MeV) = 5.23 as the mean value of the logarithm of the flux above 1 MeV. The model gives about a 23% chance of exceeding the average flux in the MeV region. Since σ (E) is monotonically increasing with energy, this probability decreases slightly at higher energies.

5

For example, the probability of exceeding the average flux above 3 MeV $(4.06 \times 10^1$ $cm^{-2}sec^{-1})$ is about 19%. This means that at the higher energies one is encountering the majority of the electrons in a smaller fraction of the time because of the stronger time dependence of the relativistic electrons.

The protons encountered in synchronous orbit will be dependent upon the activity of the sun. As was mentioned, the large flux of low energy trapped protons J (> 10 keV) = 3.5×10^7 $cm^{-2}sec^{-1}$ are not able to penetrate even the thinnest areas of the spacesuit. The flux of trapped protons above 2 MeV is exceeded by the Energetic Storm particles from the sun. The flux of extramagnetospheric protons incident at synchronous altitude depends upon the geomagnetic cutoff energy. The low altitude measurements (13) give a cutoff energy during quiet times of about 5 MeV. Since the magnetic storm associated with the arrival of the storm particles will effectively lower this cutoff energy, it is not considered pessimistic to assume a geomagnetic cutoff proton energy of 2 MeV for geostationary missions. The integral proton spectra obtained for various times during cycle 19 is shown in Figure 2. It is seen that even at solar minimum the penetrating proton environment is entirely extramagnetospheric.

The predictions of Webber (14), which were based upon an approximate correlation of yearly fluence with mean sunspot number, were used along with an assumed cutoff of 2 MeV to obtain the expected yearly fluence of protons as a function of time at synchronous altitude. This is portrayed in Figure 3 and it combines the contributions from trapped protons, ESP, SCR and GCR protons. Just as was the case for extramagnetospheric missions

6

the expected fluence in the range 10 <E< 100 MeV is critically dependent upon our ability to predict the solar particle event fluences.

Low Altitude Missions

Viable extended missions at low altitude will naturally try to avoid the intense inner zone. However, these energetic protons penetrate down into the exponential atmosphere and the planned missions must also try to minimize atmospheric drag losses. Because of the geographically non-symmetric magnetic field geometry in which these particles move, this proton penetration is confined to the South Atlantic. The scale of the asymmetry is ∿ 1000 kilometers. Thus, as we picture mission altitudes decreasing from ∿ 1000 km, we see that the mission will spend an ever increasing fraction of the time below the belts and thereby a decreasing fluence. This altitude dependence is also a strong function of incli-nation angle because of the asymmetry in magnetic latitude. Also, parti-cularly for altitudes under 300 nautical miles (∿ 550 km), the peak flux levels become strongly altitude dependent due to the exponential nature of the atmospheric losses. An appreciation for the orbital parameter dependence can be obtained from Figure 4 which displays the predicted daily fluences of the Vette API Model (protons of energy E > 34 MeV) for low altitude circular orbits.

From this discussion it is apparent that the fluence-spectral shape will be dominated by the flux spectrum in the region of the most intense flux. A mission at about 300 nautical miles altitude will encounter the most intense high energy proton flux at L = 1.3 earth radii and B = .20 gauss. This B, L point measures the deepest intrusion of the satellite into the

7

B, L space of the trapped particles. Alternatively, the mirror point trace which is given by B = .20 gauss and L = 1.3 earth radii has a minimum altitude of approximately 300 nautical miles. This B-L point is also an interesting one, because the spectrum has been subjected to a number of investigations there. In Figure 5 we present the differential spectrum at (B = .20, L = 1.3) as derived from Vette's model, API-4, and compare it with that obtained by Freden and White in their emulsion experiment (15) and that obtained in various satellite experiments.

The scatter in the data is typical for the inner zone. Since the data were taken during different epochs, it was natural to look for time dependence of the trapped protons. Freden (16) found that the analysis of the time dependence was obscured by the inaccuracies in the field model. Lindstrom and Heckman (11) confirmed that the field model inaccuracies are sufficient to provide nearly order-of-magnitude scatter in this region. At (B = .2,L = 1.3) the scatter is most severe for protons under 50 MeV. At higher L values, differences from Vette's composite model have been noted (17) which are mostly at the higher energies. However, that scatter is about the same magnitude as that presented here for the energies < 50 MeV. It is possible, although not established, that most of the scatter is due to the inaccuracies in the field model. It appears (10) that the latest field model may be accurate enough to reanalyze the data. Until this is accomplished, we must expect the model environment to represent the flux to within only a factor of 3 at best at low altitudes.

The non-isotropic nature of the flux is also a source of scatter besides being of significance to hazard evaluation in non-uniform shielding configurations. In Figure 6, we present the omnidirectional integral spectrum J, and the unidirectional integral spectrum $J_\perp$ perpendicular to the field at B = .20 and L = 1.3 as given by API-4. For visualization $4 \pi J_\perp$ is also given as a dashed curve. It is seen that in the energy range from 10 to 100 MeV roughly 1/4 the solid angle contains all the flux. At higher energies the proton flux is even more anisotropic. In addition, the higher proton energies have a sufficiently large radius of gyration to develop a significant east-west asymmetry. For example, a mirroring 100 MeV proton arriving at a spacecraft at B = .2 from the east has just interacted with the atmosphere nearly 150 kilometers below. This will cause an east-west asymmetry of greater than 50%. The important feature for hazard evaluation is that the unidirectional flux in the eastern section is roughly 3 times its average value for a vehicle geographically oriented in the South Atlantic anomoly. For a geomagnetically oriented vehicle the asymmetry in the fluence will be greater.

For a concise study of the radiation hazard to extended missions at low altitudes, we have chosen a 260 nautical mile altitude. The severity of the environment may call for a reduction in the altitude, however, to consider altitudes as low as 200 nautical miles introduces substantial costs due to drag losses. An intermediate inclination angle of 50° is chosen to establish the significance of the geomagnetic cutoff to the extramagnetospheric radiation environment contributions.

The omnidirectional trapped-proton fluence-spectrum for this mission is
presented in Figure 7 as derived from the API-4 model. The electron
fluence spectrum predicted for the post-1968 period is portrayed in Figure
8. The steepness of this spectrum is due to a quite significant contri-
bution from the outer zone electrons. However, there is a remnant of the
Starfish injection. Thus, this prediction is considered to be on the
conservative side provided that no further high altitude tests are made.

The galactic cosmic ray and solar particle event environments encountered
by the mission will have the variations and modulations that were described
in (1). In addition, they will be modified by the geomagnetic field.
Particles with insufficient rigidity are unable to reach a given point
inside the magnetosphere. An effective cutoff can be defined (18) for
particles to penetrate to an L shell (i.e., an invariant latitude Λ,
cos Λ = 1/L). Figure 9 summarizes the results of Webber (18) and
Bingham (13) on the effective cutoff rigidity. It is seen that the
measured cutoffs fall below the calculated values using a field based
largely upon surface measurements. In addition, a disturbance field D_{st}
of 100 gamma gives a quite significant lowering of the cutoffs. Note
that D_{st} = 100 is sufficient to reduce the cutoff at L = 6.6 to below
2 MeV. In order to transfer these data into a spectral modification for
the mission, we have calculated the fraction of the time the vehicle will
spend above a given invariant latitude. This fraction can be interpreted
as the fraction of the particles in the extramagnetospheric spectrum at
the cutoff rigidity which will be encountered by the mission. A typical
average disturbance field of 100 gamma is assumed for the events. We
have calculated the encountered fraction for this case, for quiet times

and for that given by the calculated cutoff. These are presented in Figure 10, as the geomagnetic transmission factors for the mission. Since the results are given as a function of the nucleon energy, the proton transmission factors differ from those of the helium and heavier ions. The quiet time transmission factors for polar missions are given also for comparison. It is seen that the transmission factors for the mission are a strong function of nucleon energy in the region $10 < T < 10^3$ MeV/nucleon. These transmission factors applied to the extramagnetospheric environment give the GCR and SCR environments for the mission.

SHIELDING ANALYSIS

Synchronous Altitude

The trapped radiation encountered at synchronous altitudes consists principally of energetic electrons and protons. As discussed in the previous section, the characteristic energy spectrum of the trapped protons drops off so rapidly that no significant fluxes of protons above a few MeV are encountered. This means that these protons pose no direct radiation threat to the space-suited astronaut, and their penetration characteristic will not be considered. The trapped electrons, however, are both more penetrating than the protons and are also producers of highly penetrating bremsstrahlung. To treat the complex problem of electron transport in spacecraft shields a Monte Carlo code was developed at Boeing by B. W. Mar (19). The results of this code were used to study electron penetration and bremsstrahlung production, and methods to analyze the penetration and bremsstrahlung production of the trapped electrons were developed (20, 21).

In Figure 11, we show the yearly average doses from penetrating electrons and their induced bremsstrahlung in an aluminum shield. We assume that the electrons are incident normally on the shield, thereby introducing a conservative factor of nearly 2 in the dose calculation. We note first the radically differing attenuation characteristics of the electrons and the bremsstrahlung. This leads to the well known result that, for surface doses, the penetrating electrons dominate in dose production for shielding thickness below about 0.8 g/cm^2 and the bremsstrahlung dose dominates above this thickness. At deep body points, of course, the bremsstrahlung dominates for any shielding thickness. The practical implications of these results are that present manned spacecraft will provide adequate shielding from penetrating electrons, but that the bremsstrahlung will present problems. A bremsstrahlung dose rate of nearly one rad per day is a significant radiation hazard, and means of reducing this dose will be sought. For example, an exterior shield of a material with lower atomic number than aluminum could reduce the intensity of bremsstrahlung generated.

If extra-vehicular activity is planned, the spacesuit shielding of, typically, 0.2 g/cm^2 means that high electron skin doses could be received. A skin dose of 100 rads/hr results from the average environment assuming effective body shielding over 2π steradians. However, the violent temporal variations in the flux noted previously would make it necessary to consider both the local time and the preceding solar activity before EVA was attempted.

The bremsstrahlung dose rate would also show similar fluctuations, so it must not be supposed that the yearly dose is received at a constant dose rate. One should also be aware of the pitfalls encountered when attempting to determine the shielding of a heterogeneous spacesuit material. With the penetrating electron dose such a strong function of thickness, average thickness values are not adequate to describe the shielding characteristics of a spacesuit.

Low Earth Orbit

The energetic particle environment encountered in a 260 nautical mile circular orbit is naturally divided into two components, the trapped radiation encountered principally in the South Atlantic anomoly, and those GCR and SCR which can penetrate the earth's magnetic field and reach the spacecraft's orbit. The trapped protons and electrons have a greater fraction of high energy particles than is found at synchronous altitude, and thus the radiation is more penetrating. This effect is most pronounced for the protons as their maximum energy is extended from the few MeV at synchronous altitude to many hundreds of MeV at 260 nautical miles. While the electron spectrum encountered in low earth orbit is also harder than at synchronous altitude, the differences in penetration are not as great as for the protons.

In Figure 12 we show the depth-dose profiles resulting from the incident protons. The code used to obtain these results is described in (20). Several modifications made in this contract and the dose definitions are described in this report in the following section. The dose rates reported are long term averages, and do not reflect the peak dose rates encountered

13

in the heart of the South Atlantic anomoly. The dose rates are also those resulting from an omnidirectional flux. The angular dependent dose rate can be estimated from the results of the previous section on the near earth environment. The direct ionization from the incident protons is the dominant energy deposition mechanism throughout the range of shielding thicknesses considered, with cascade protons ranking second in importance. It should be carefully noted, however, that as the proton differential energy spectrum has not been determined in detail above 100 MeV, the shape of the dose curve depends on the accuracy of the representation in Figure 7. Data from an Air Force experimental satellite (17) indicates that the situation is complex. Finally, we note that for a typical spacecraft shielding of 2.0 g/cm^2, the average dose rate is nearly 0.5 rads/day for point doses.

The electron and bremsstrahlung doses shown in Figures 13-14 show the same general behavior as those predicted at synchronous altitude, though the electron and bremsstrahlung are more penetrating. EVA activity would incur an average dose of 100 rads/day skin dose in a spacesuit of 0.2 g/cm^2 shielding. Avoidance of the South Atlantic anomoly in normal EVA would seem a reasonable way to minimize these radiation problems.

In Figure 15 we show the fraction of each dose component received under 5 g/cm^2 of aluminum that results from incident proton energies of energy E or greater. In Figure 16 the differential dose distribution, defined in (1), found under shielding thickness of 1 and 5 g/cm^2 is shown. The differential dose distribution, shown in Figure 16 plotted per logarithmic

increment in interior energy, emphasizes the dose contributions from higher proton energies by compression of the energy scale. In Figure 17 the percent of the total dose delivered by protons in 20 MeV increments is shown for 1 and 5 g/cm^2 of aluminum shielding. This representation of the same physical situation as shown in Figure 16 shows the importance of the low energy protons of the 260 nautical mile proton spectrum in producing dose.

EVALUATION OF HIGH ENERGY (> 400 MeV) PROTON
INDUCED SECONDARIES

In (1), the evaluation of proton induced secondary particles was restricted to interacting proton energies of less than 400 Mev by the lack of nuclear interaction data. While this restriction did not appear important for the low rigidity Solar Cosmic Ray (SCR) events, it is obviously necessary to extend the dose calculation to include the higher energy protons of the incident proton spectra for the galactic cosmic rays and high rigidity proton events. In this study the Boeing Secondary Proton code was used with the preliminary data on high energy interactions developed by Bertini, (22), to extend the treatment of proton induced secondaries from 400 MeV to 2000 MeV.

DESCRIPTION OF DOSE COMPONENTS FROM THE BOEING SECONDARY PROTON CODE
The Boeing Secondary Proton Code is described in (1) and (20), and only the basic dose definitions and a recent change in neutron transport and dose calculation will be presented in detail. The dose components presented in this report are defined as follows, all doses being in tissue rads:
1. Primary proton dose - the ionization dose resulting from incident protons which have not been involved in nuclear reactions. The energy removed from the proton beam at the dose point by ionization energy losses is assumed equal to the dose at that point. Delta ray transport is not considered.

2. Cascade Proton Dose - the ionization dose resulting from those protons, both cascade and evaporation, that result from the inter- action of the primary protons and secondary neutrons with the nuclei of the shield.

3. Neutron dose - the dose resulting from neutron - proton elastic scattering in tissue. The energy of the scattered proton is assumed deposited at the scattering site.

4. Proton Heavy Particle Dose - the kinetic energy acquired and locally deposited by the recoiling nucleus, and by evaporating charged particles heavier than protons, as a result of the non- elastic collision of an incident proton with a tissue nucleus.

5. Neutron Heavy Particle Dose - the kinetic energy acquired and deposited locally by the recoiling nucleus, and evaporating charged particles heavier than protons, as a result of the non- elastic collision of a secondary neutron with a tissue nucleus.

One significant change has been made in the calculations since the work reported in (1) was presented. The neutron dose, which was previously estimated by the energy removal cross section of Gibson (23), is now treated more completely by following the tertiary protons produced by the neutrons. This allows a more accurate estimate of the dose, as well as a detailed description of the way in which the dose is being deposited. In Figure 18 we give a comparison of the results of the latest version of the Boeing code with the results of the Oak Ridge Nucleon Transport Code. The agreement has improved from that obtained in the previous report (1).

INCORPORATION OF BERTINI'S HIGH ENERGY MONTE CARLO RESULTS

Preliminary data from Oak Ridge National Laboratory on high energy nuclear interactions (22), are now available. While these data cover only a few incident particle energies and target elements, it was felt worthwhile to make dose estimates for the high rigidity SCR events and the galactic cosmic-ray protons. Although the final interaction data may differ slightly from the preliminary data used in this work, it is unlikely that the final dose results will be significantly affected. The Bertini data has been smoothed to meet the input requirements of the Boeing code. In addition, as only incident proton energies of 750, 1000, and 2000 MeV were reported, considerable interpolation between energies was required.

As the Boeing code does not treat pions, the pion production data are not used, and no pion doses are estimated. Early calculations, based on cosmic ray data, by Alsmiller (24) indicated that the pion dose contribution should be small for shielding thicknesses of less than 100 g/cm^2 of aluminum, and for incident energies up to 2 GeV. While the SCR spectra fall off rapidly enough that the particle energies above 2 GeV are of little importance in these dose calculations, the galactic cosmic ray proton energy spectra may be hard enough to make particle energies above 2 GeV contribute a significant amount to the total dose. The dose estimates given in the following sections of this report utilize the new high energy proton data, and the calculation of both primary and secondary doses extend out to 2 GeV.

REVISED GALACTIC COSMIC-RAY PROTON DOSE CALCULATION

In Figure 19 we present the dose rates resulting from the galactic cosmic-ray proton spectrum at solar minimum incident normally on a slab of aluminum. As the straightahead approximation is used throughout the calculation, one may also regard the dose rate under a given slab thickness, x, of aluminum as being numerically equal to that received at the center of a spherical shell of wall thickness, x, exposed to an isotropic flux of galactic cosmic-ray protons. Also only slab thicknesses less than an interaction mean free path, 93.8 g/cm^2 in aluminum, are given. For greater thickness, the first collision approximation and the straightahead approximation used in the calculation become less appropriate.

Looking at the dose results, we note that the primary proton and cascade proton dose components dominant in the entire range of shielding thicknesses considered. The total dose is nearly constant, increasing slightly in the first few g/cm^2 and then falling off very slowly. The primary proton and cascade proton doses are both characterized by a low average LET. The neutron, primary heavy particle, and neutron heavy particle rad doses are down by an order of magnitude from the sum of the two proton components. However, the much higher average LET for these dose components suggest that they should be carefully considered in determining the biological implications of the galactic cosmic rays.

The inclusion of secondary interactions of protons up to 2 GeV gives a much more complete picture of the dose distribution resulting from the GCR protons. We feel that the secondary interactions above 2 GeV would

probably add enough to the total dose to give a more pronounced
buildup of the dose. Work is underway to check these dose estimates
with the observed ionization rate in the atmosphere.

In Figure 20 the fraction of each dose component received under 10 g/cm^2
of aluminum resulting from incident protons of energy E or greater is
shown. It is interesting to note that 50% of the cascade proton dose
comes from incident protons with energy less than 1 GeV.

HIGH RIGIDITY SOLAR PROTON DOSE CALCULATION

The high energy data were also used to evaluate the importance of the
proton energies above 400 MeV in Solar Cosmic Ray events. The expo-
nential rigidity representation for the energy spectrum of the Solar
Cosmic Rays has been found to require a very high range of charac-
teristic e-folding rigidity, P_o, to cover all the recorded events.
In a recent article (25), a P_o of 600 Mv was found to best represent
the data on the early portion of the January 29, 1967, solar particle
event. In contrast, P_o's of 5 and 10 Mv have been used to describe the
Energetic Storm Particle phase of some solar particle events.

In Figures 21 through 26, we present depth-dose profiles for charac-
teristic rigidities ranging from 40 Mv to 600 Mv. These results differ
from those of (1) in that first the neutron dose is calculated in the
improved manner previously noted, and   second the high energy inter-
actions are included. For the 40 Mv spectrum, the neutron dose is
reduced, below that calculated in (1), while the cascade proton dose is
increased. In fact, at 35 g/cm^2 the cascade proton dose is equal to the
primary proton dose, a circumstance resulting from the contribution of

the neutron-produced cascade-tertiary protons. The proton and neutron heavy particle doses are so low as to be negligible. The primary proton dose is unchanged. The same general trend is apparent in the 100 Mv spectrum results, Figure 22, an increase in the cascade proton dose and a decrease in the neutron dose as compared to the previous estimates.

For the 160 Mv spectrum (Figure 23) we present a comparison between the results obtained with a 400 MeV cutoff (dashed lines) and a 2 GeV cutoff on secondary particle production (the present treatment). The primary proton dose remains essentially unchanged over the complete range of shielding thicknesses presented. The cascade proton dose is seen to be about 15% low at 50 g/cm^2 if the high energy interactions are neglected. The neutron dose remains essentially constant, which implies that the lower energy incident protons result in nearly all of the neutron dose. The heavy particle doses are both strongly affected by the inclusion of the high energy data. The results for the 200 and 400 Mv spectrum show a trend which culminates in the 600 Mv spectrum. At 600 Mv, it is seen that the high energy data strongly affects all dose components. It is obviously necessary to include the high energy proton interactions for a complete dose description. As in the case of the galactic cosmic rays, the primary and cascade proton doses dominant the rad-dose estimate, but the high LET neutron dose and the proton and neutron heavy particle doses must be considered in determining the biological implications of these particle events.

SECONDARY DOSE CONTRIBUTION FROM HEAVY IONS
IN THE GALACTIC COSMIC RADIATION

Although protons constitute the largest proportion of incoming galactic particles, heavier particles are present and we have previously calculated that particles heavier than protons account for some 60% of the free space dose from galactic cosmic rays (1). As they penetrate the spacecraft and bodies of the astronauts, they will interact and fragment into lighter particles with less charge but with greater range than the initial particles. It is of considerable interest to estimate this contribution as a function of depth to determine its relative importance to the total dose deposited. Such heavy primaries and their secondary heavy fragments are of additional biological interest because their highly ionizing character will cause irreparable damage which may accumulate in some organs and eventually cause functional damage on long missions.

A calculation is presented here of the secondary contribution from a primary neon ion (Z = 10) with incident energy of 300 MeV/nucleon. The maximum of the cosmic ray differential energy spectrum occurs at this energy. It is not difficult to see how this procedure could be generalized so that the contributions from various primary ions with different energy spectra could be calculated by means of an appropriate computer code.

As indicated previously, secondary production data from protons in the important energy region 400 - 2000 MeV have only recently become

available. From the theoretical point of view, the proton-nucleus interaction is complex and considerable effort was necessary to produce meaningful data on secondary production starting from basic nucleon-nucleon cross sections (22). The problem becomes even more complex when the incident particle is also a nucleus consisting of several bound nucleons. Little theoretical progress has been made in understanding the important mechanisms causing the fragmentation of such heavy ions in the energy range of interest (100 - 10,000 MeV/nucleon).

THE COSMIC RAY EMULSION DATA

A small amount of data, however, is available in the high energy region from cosmic ray experiments in nuclear emulsion. It was decided to utilize these data to arrive at estimations of emission frequencies for the various secondary particles emerging from a heavy ion-nucleus interaction.

The compilations used were those of Fowler, Hillier and Waddington (26), and Rajopadhye and Waddington (27). In these compilations, the incoming ion was charge-identified and the following information was tabulated on each interaction: the number of slow prongs, the identity of the fast outgoing heavy fragment ($Z > 2$) in the forward direction (if any), the number of fast alpha-particles (in the forward direction), and the number of "shower" particles (pions, fast protons, etc.). For the purpose of estimating emission frequencies in nuclei constituting tissue (H,C,N,O), all interactions producing more than seven slow prongs were eliminated. This eliminated all obvious interactions involving silver and bromine nuclei in the emulsion. All interactions with seven or

fewer slow emerging prongs were accepted. This undoubtedly included some heavy nucleus interactions in which only a few slow prongs emerged, but it is felt that this contamination is small.

The data on the heavy fragment emission frequencies are shown in Figure 27. The total number of interactions represented here is 382 and includes data from primaries of boron (Z = 5) through magnesium (Z = 12). Although there is little data on each ion, it is seen that the overall picture is reasonably consistent with the assumption that, for a given primary, there is about a 10% probability that any lower massed fragment (heavier than an alpha-particle) will emerge from an interaction. Thus, 10% was chosen as an approximation of the emission frequency for any secondary heavy fragment from a neon ion-nucleus interaction. The average number of fast alpha-particles per interaction was 1.04. The average number of "shower" particles was 6.34.

ASSUMPTIONS MADE IN THE CALCULATION

The dose calculation was made for a 300 MeV/nucleon neon ion incident on a water absorber (range - 10 cm). A number of assumptions were made so that the calculation could be made in a straightforward manner. They are as follows:

1. The heavy fragment (if any) leaving the interaction site was assumed to be the residual piece of the incident particle and was assumed to continue in the forward direction with the same velocity as the incident particle. The reported rms angles for the emerging heavy fragments were 0.48^{o} from incident particles with 6< Z <9 and 1.14^{o} from incident particles with Z > 9, so the straightahead approximation

is certainly warranted in this case. It is not clear how much error is introduced by assuming the fragment has the same velocity as the incident particle. The small emission angle plus the lack of velocity change is consistent with a model in which part of the incoming particle is just stripped away in the collision, with the remaining fragment continuing on with little change in direction or velocity.

2. The fast alpha-particles were also assumed to continue in the forward direction with the same velocity as the incident particle. The rms angles of these alpha-particles ranged from 1.1° to 2.5° for the various incident charged components (26). Here again, it is assumed that since the angle of emission is small, the velocity change between the incident particle and the outgoing alpha-particle is small and has here been set equal to zero.

3. The residual "star" at the interaction site can be treated as if it were a pion star (28) depositing locally 30 MeV per interaction. This assumption is not critical, because so little dose is deposited in this way. A factor of two or four increase in this number would not affect the total dose from the secondaries appreciably except at the surface, where the secondary dose is very low anyway.

4. The "shower" particles, which in the cosmic ray data consist of fast protons, deuterons, tritons, pions, kaons, muons, and electrons, will contribute most of their dose as minimum ionizing particles, which is negligible for this case. As a reasonable upper limit, we assume that this contribution consists entirely of protons travelling in the forward direction with velocity equal to that of the incident particle, but with an emission frequency one half of that measured in

25

the cosmic ray data. It will be seen that this contribution is on the same order of magnitude as the alpha-particle contribution and will affect the total secondary dose appreciably only at very great depths, where the total secondary dose is again low.

5. The interaction cross section was assumed constant as a function of energy.

6. Tertiary interactions were neglected.

THE SECONDARY DOSE CALCULATION

The energy deposited per gram per incident ion/cm^2 at point x from secondaries of the ith type (e.g., alpha-particles) is given by

$$D_i(x) = K_i \int_0^X (dn/dx') (dE/dx(x,x')_i) \, dx'$$

where K_i = number of particles of the ith type emerging per interaction; the emission frequency

X = the range of the primary ion (10 cm in this case) or x, whichever is smaller

dn/dx' = number of interactions per unit length

= $\exp(-x'/\lambda)/\lambda$ where λ is the nuclear interaction mean free path = 16.7 g/cm^2 in this case

$dE/dx(x,x')_i$ = the ionization dE/dx at point x of a particle of type i created at x' with the same energy/nucleon that the primary had at x'.

The total secondary dose at x is

$$D_{TOTAL}(x) = \sum_i D_i(x) + D_{STAR}(x) + D_{SHOWER}(x)$$

where $D_{STAR}(x) = 30 \exp(-x/\lambda)/\lambda$ MeV/g-ion/cm^2 (for $x \leq 10$ cm)

$D_{SHOWER}(x) = D_{PROTON}(x)$ with $K_{PROTON} = 3.17$

It is convenient to plot the secondary dose as a percentage of the incident primary dose (at the surface). For the case in question, the incident primary dose is 357 MeV/g per incident ion/cm^2. The percentages for fluorine, nitrogen and helium secondaries are shown in Figure 28 as a function of depth in water. The total secondary contribution is also shown.

CONCLUSIONS

The work described in this report makes it possible to draw several conclusions about our present knowledge of the radiation environment encountered in the magnetosphere, and the properties of these radiations behind various shielding thicknesses.

The high energy data from Oak Ridge serves to extend our understanding of the proton induced secondary doses from galactic, solar and trapped protons. We have also suggested a way in which the importance of the galactic heavy particle secondary doses can be estimated. We list here the major conclusions we draw from this study.

1. The radiation environments encountered by extended orbiting missions are subjected to major uncertainties. At synchronous altitudes the environment is strongly time dependent. The AE3 model of the trapped electrons, the best available for the long term missions, is dominated by the solar cycle variation of the solar particle events that is (at best) poorly determined.

2. The major contribution to the penetrating environment at low altitudes is the inner zone protons. The uncertainty in the flux of these trapped protons is about a factor of 2 to 3, which in large measure may be due to the inaccuracy of the geomagnetic field model employed in the data reduction where the flux is a strong function of B and L. For mid-inclination orbits, the solar particle event contribution at low altitudes is a sensitive function of the disturbance field as well as the spectra and intensities of these events.

3. The radiation hazards to man at synchronous altitude come from the galactic and solar cosmic rays as well as the trapped electrons. The effective magnetic cutoff energy is low enough that the solar and galactic cosmic ray environment is essentially the same as that encountered outside the magnetosphere. The trapped electrons are of sufficient intensity to provide a radiation hazard to EVA through direct penetration, and through spacecraft shielding by bremsstrahlung. Strong time variations in the electron flux, related to both local time and solar activity must be considered in planning mission activities.

4. At 260 nautical mile altitude the solar and galactic cosmic rays are strongly modified by the earth magnetic field. Depending on the inclination of the orbit, the spacecraft will encounter differing fractions of the deep space particle fluxes. The trapped protons encountered in the South Atlantic anomoly provide the principal continuing radiation hazard inside a spacecraft, and the yearly dose rates are high enough, 175 rads/year under 2 g/cm^2 of aluminum, to command attention. The protons of energy ranging from 10 to 100 MeV at the dose point are depositing a large fraction of the total dose under shielding thicknesses of 1 to 10 g/cm^2 of aluminum. For EVA, penetrating electron skin doses near 100 rads/day can be expected under 0.2 g/cm^2 of aluminum, suggesting that EVA during anomoly passage should be avoided.

5. The high energy data from Oak Ridge National Laboratory has enabled us to better describe the high rigidity solar cosmic ray and galactic cosmic ray proton dose characteristics. Of the many features of the

29

dose characteristics shown, the possible importance of the heavy evaporation and nuclear recoil doses in determining delayed biological effects seems of particular interest. It would seem that interaction data ranging up to 2.0 Gev is adequate to describe the dose characteristics of the solar cosmic rays. The galactic cosmic ray protons require even higher energy interaction data to complete the dose description.

6. A method has been developed for evaluating the secondary dose from a heavy galactic cosmic ray particle at one incident energy. This method can be extended to treat the galactic heavy particle spectra and provide an estimation of the secondary contribution from this component.

REFERENCES

1. S. B. Curtis and M. C. Wilkinson, "Study of Radiation Hazards to Man on Extended Missions" NASA CR-1037, May 1968

2. B. M. McCormac, (Ed), Radiation Trapped in the Earth's Magnetic Field Gordon and Breach, New York, N.Y., 1966

3. K. A. Anderson, "Energetic Particles in the Earth's Magnetic Field," Annual Reviews of Nuclear Science, Vol 16, 291, (1966)

4. R. W. Filkins, "Trapped Protons of the Inner Radiation Belt," J. Geophys. Res. 71, 97 (1966)

5. J. I. Vette, "Models of the Trapped Radiation Environment, Volume I: Inner Zone Proton and Electrons" NASA SP-3024 (1966)

6. J. I. Vette and A. B. Lucero, "Models of the Trapped Radiation Environment, Volume III: Electrons at Synchronous Altitude" NASA SP-3024 (1967)

7. J. H. King, "Models of the Trapped Radiation Environment, Volume IV: Low Energy Protons" NASA SP-3024 (1967)

8. S. C. Freden and R. S. White, "Protons in the Earth's Magnetic Field," Phys. Rev. Letters, 3, 9 (1959)

9. C. E. McIlwain, "Coordinates for Mapping the Distribution of Magnetically Trapped Particles," J. Geophys. Res. 66, 3681 (1961)

10. A. Hassitt, "The Drift Velocity of Trapped Particles," J. Geophys. Res. 70, 535 (1965)

11. P. J. Lindstrom and H. H. Heckman, "B-L Space and Geomagnetic Field Models" J. Geophys. Res. 73, 3441 (1968)

12. D. C. Jensen and J. C. Cain, "An Interim Geomagnetic Field" J. Geophys. Res. 67, 3568 (1962)

13. R. G. Bingham and W. R. Webber, "Direct Measurements of Geomagnetic Cutoffs for Cosmic Ray Particles in the Latitude Range $\lambda = 45^{\circ}$ to 70° Using Balloons and Satellites," (A paper presented at the tenth International Conference on Cosmic Rays - Calgary, Alberta, Canaca, June 1967) Boeing Document D2-114037-1, July 1967

14. W. R. Webber, "Sunspot Number and Solar Cosmic Ray Predictions for Cycle 20 (1965-1975) with Preliminary Estimates for Cycle 21" Boeing Document D2-113522-1, May 1967

15. S. C. Freden and R. S. White, "Trapped Proton and Cosmic Ray Albedo Neutron Fluxes," J. Geophys. Res. 67, 25 (1962)

16. B. M. McCormac, Editor, Earth's Particles and Fields, p. 3, Reinhold Book Company, New York, New York, 1968

17. A. L. Thede, G. E. Radke, "Correlation of Dosimetric Measurements with Charged Particle Environment of Inner Van Allen Belt" NASA-SP-169, p. 75-92, 1968.

18. W. R. Webber, "Diurnal Variation of Intensity and Energy Spectrum of Low-Energy Electrons Incident at Fort Churchill, Canada" J. Geophys. Res. 73,4905 (1968)

19. B. W. Mar, "Electron Shielding Codes for Evaluation of Space Radiation Hazards," Boeing Document D2-90414,June 1963

20. J. A. Barton and B. W. Mar, "Computer Codes for Space Radiation Environment and Shielding," WL TDR-64-71, Vol. 1., Air Force Weapons Laboratory, August 1964

21. B. W. Mar, "The Calculation of Bremsstrahlung Radiation Penetrating a Space Vehicle" Boeing Document D2-90411, June 1963

22. Hugo W. Bertini, "Preliminary Data from Intranuclear-Cascade Calculations of 0.75-, 1.0- and 2.0 GeV Protons on Oxygen, Aluminum, and Lead, and 1.0 GeV Neutrons on the Same Element," ORNL-TM-1996, December 1967

23. W. A. Gibson, "Energy Removed from Primary Proton and Neutron Beams by Tissue," ORNL-3260, 1962

24. R. G. Alsmiller, Jr. and J. E. Murphy, "Calculations of the Attenuation of a Model Solar Flare and Monoenergetic Proton Beams by Aluminum Shields, " ORNL-3317, January 1963

25. J. A. Lockwood, "Cosmic-Ray Solar Flare Effect of January 28, 1967, as Recorded by Neutron Monitors," J. Geophys. Res. 73, 4247, (1968)

26. P. H. Fowler, R. R. Hillier and C. J. Waddington; Phil. Mag. 2, 293 (1957)

27. V. Y. Rajopadhye and C. J. Waddington; Phil. Mag. 3, 19 (1958)

28. P. H. Fowler; Private Communication (1967)
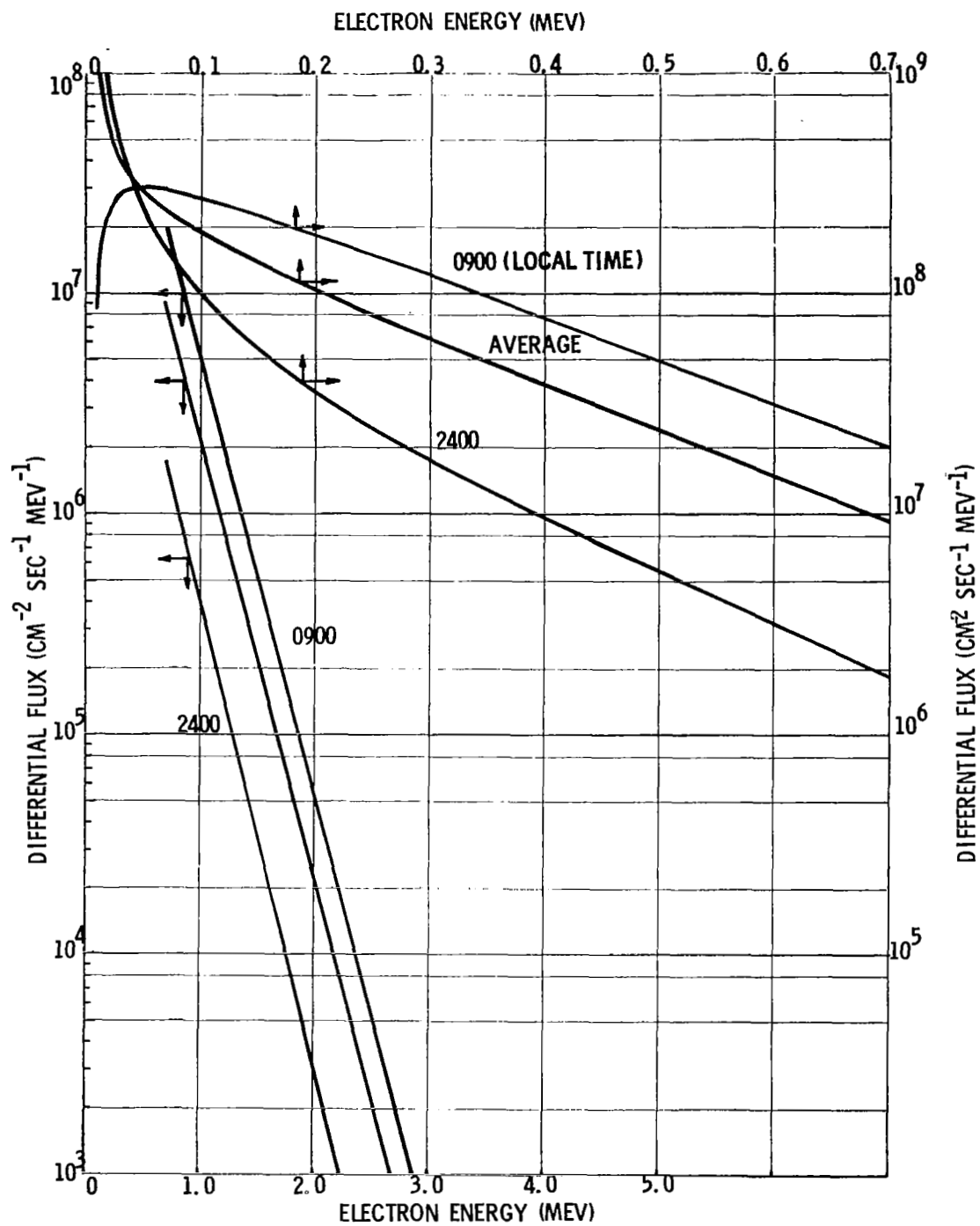
Figure 1

DIURNAL EXTREMES AND THE LOCAL TIME AVERAGE OF THE
MEAN ELECTRON SPECTRUM AT SYNCHRONOUS ALTITUDE

33
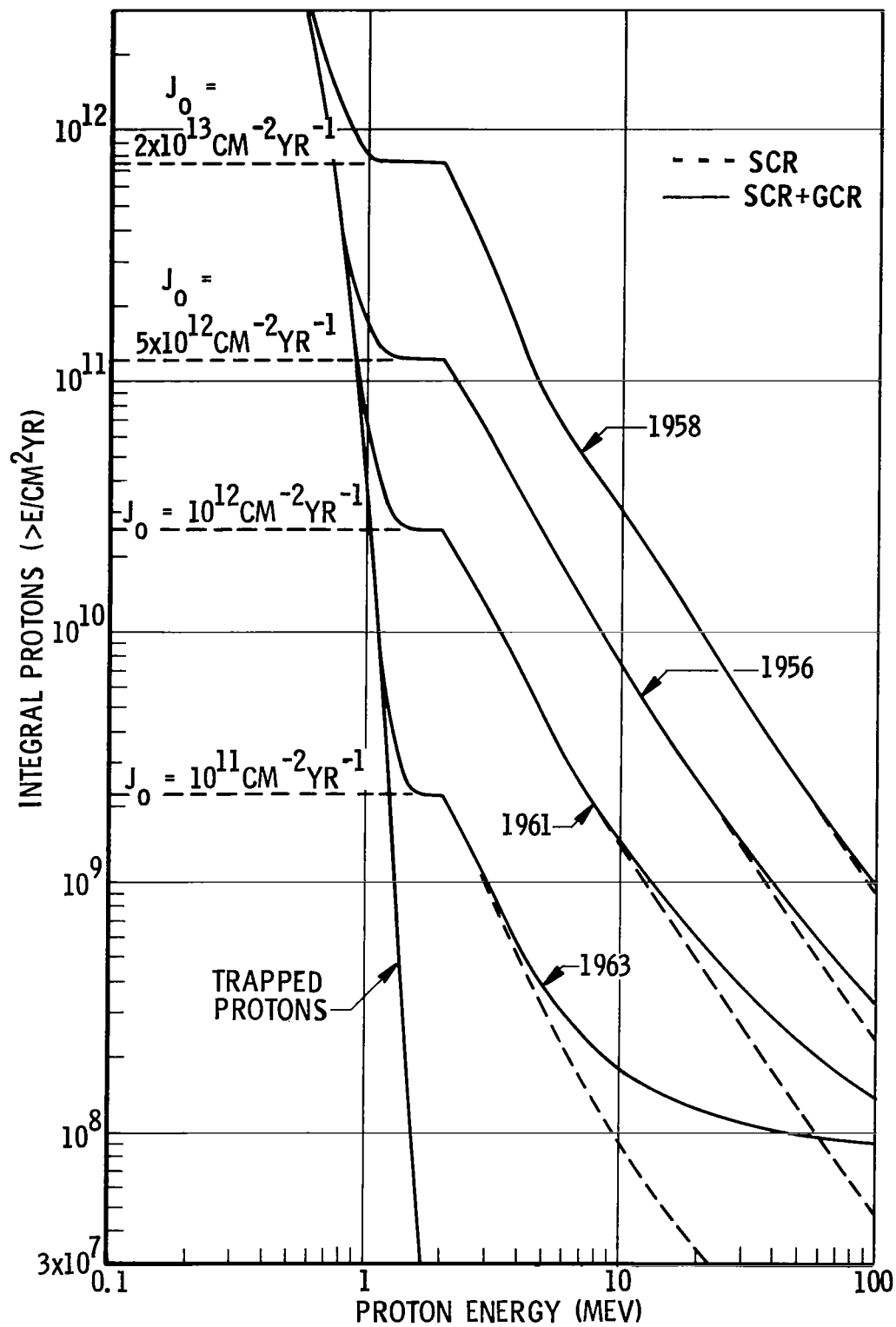
FIGURE 2: SYNCHRONOUS ALTITUDE PROTONS DURING
SOLAR CYCLE 19
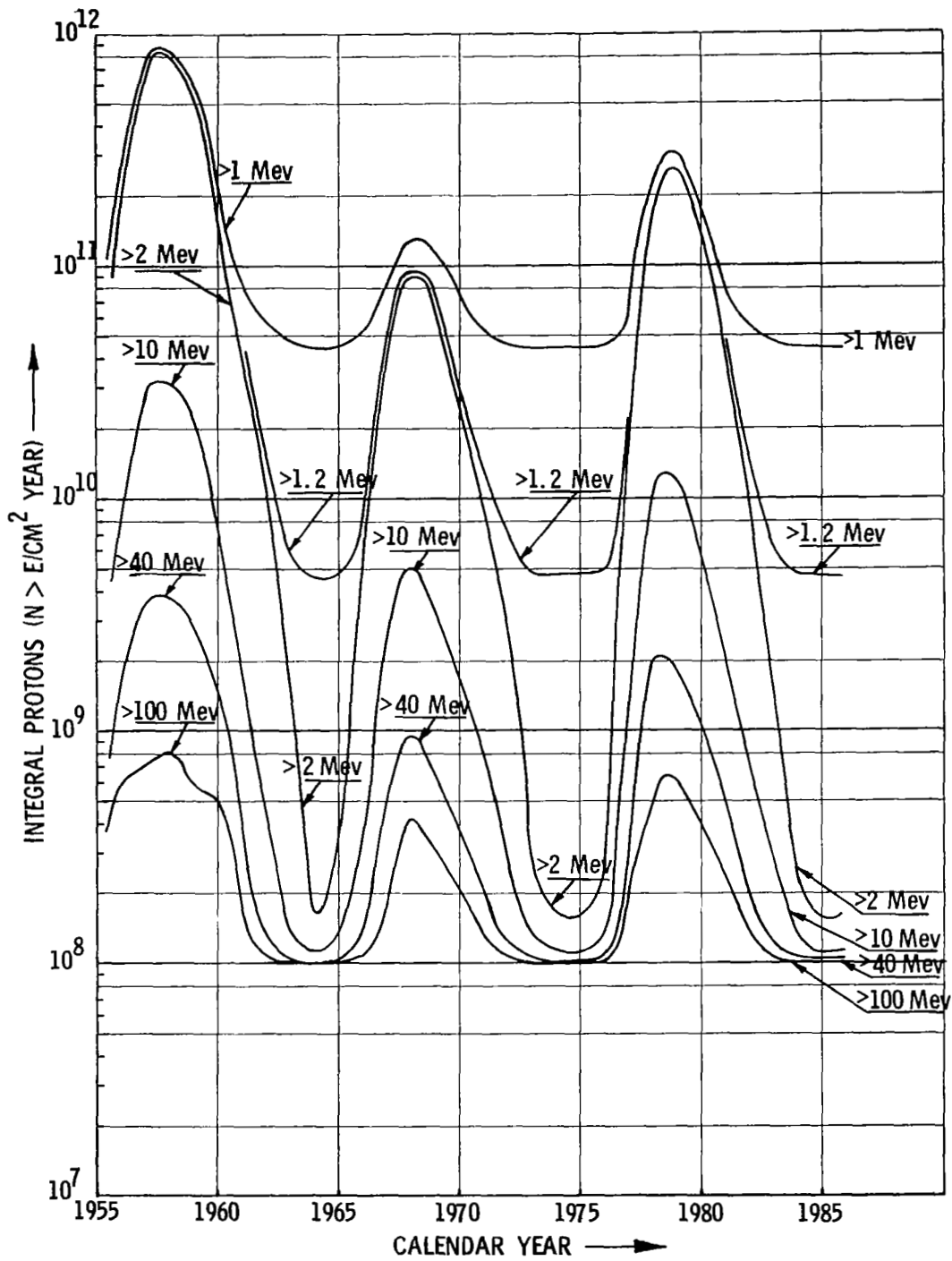
FIGURE 3

PREDICTED INTEGRAL PROTON FLUENCES FOR
GEOSTATIONARY MISSIONS
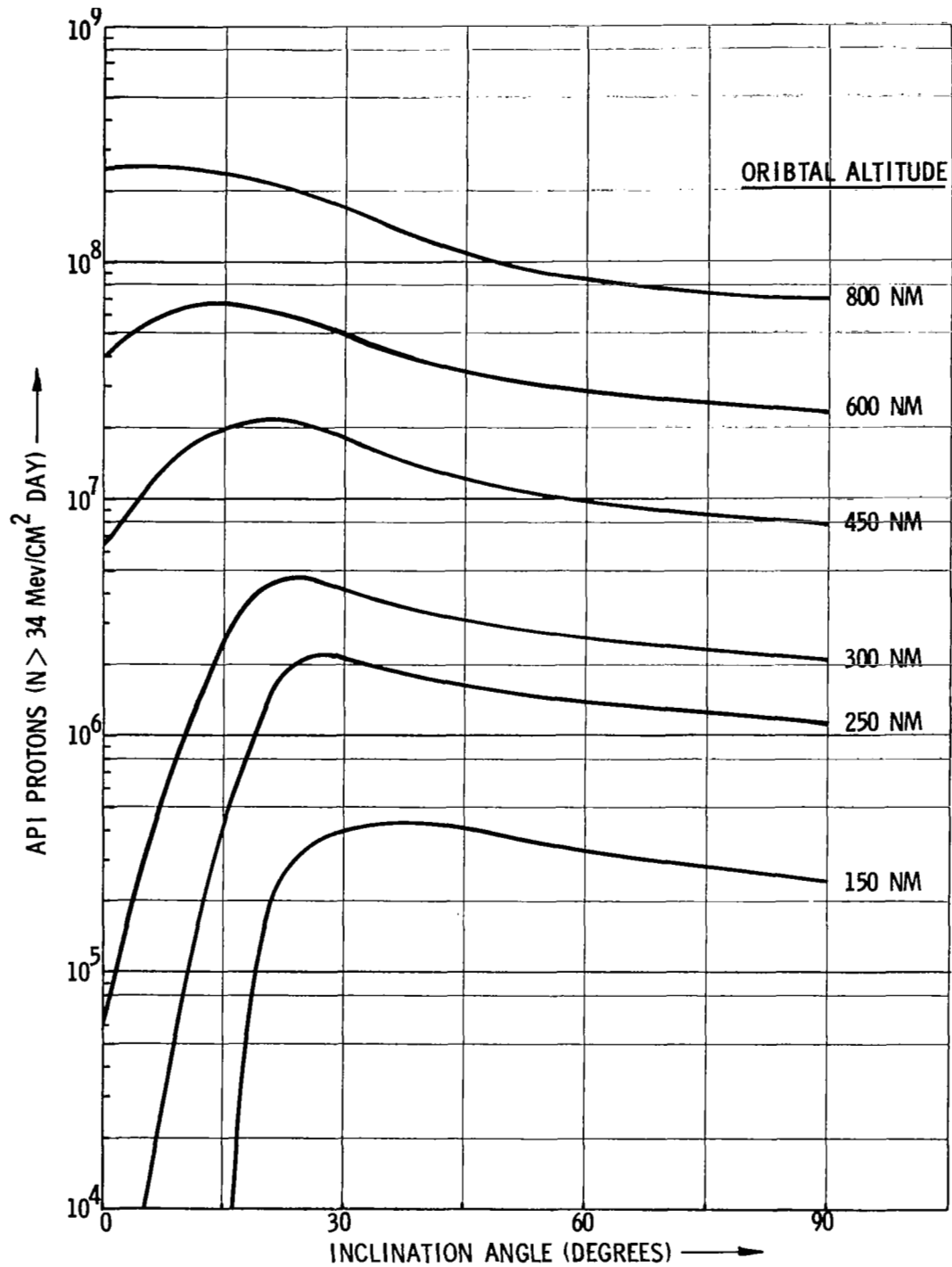
Figure 4

LOW ALTITUDE PROTON FLUENCE ABOVE 34 Mev
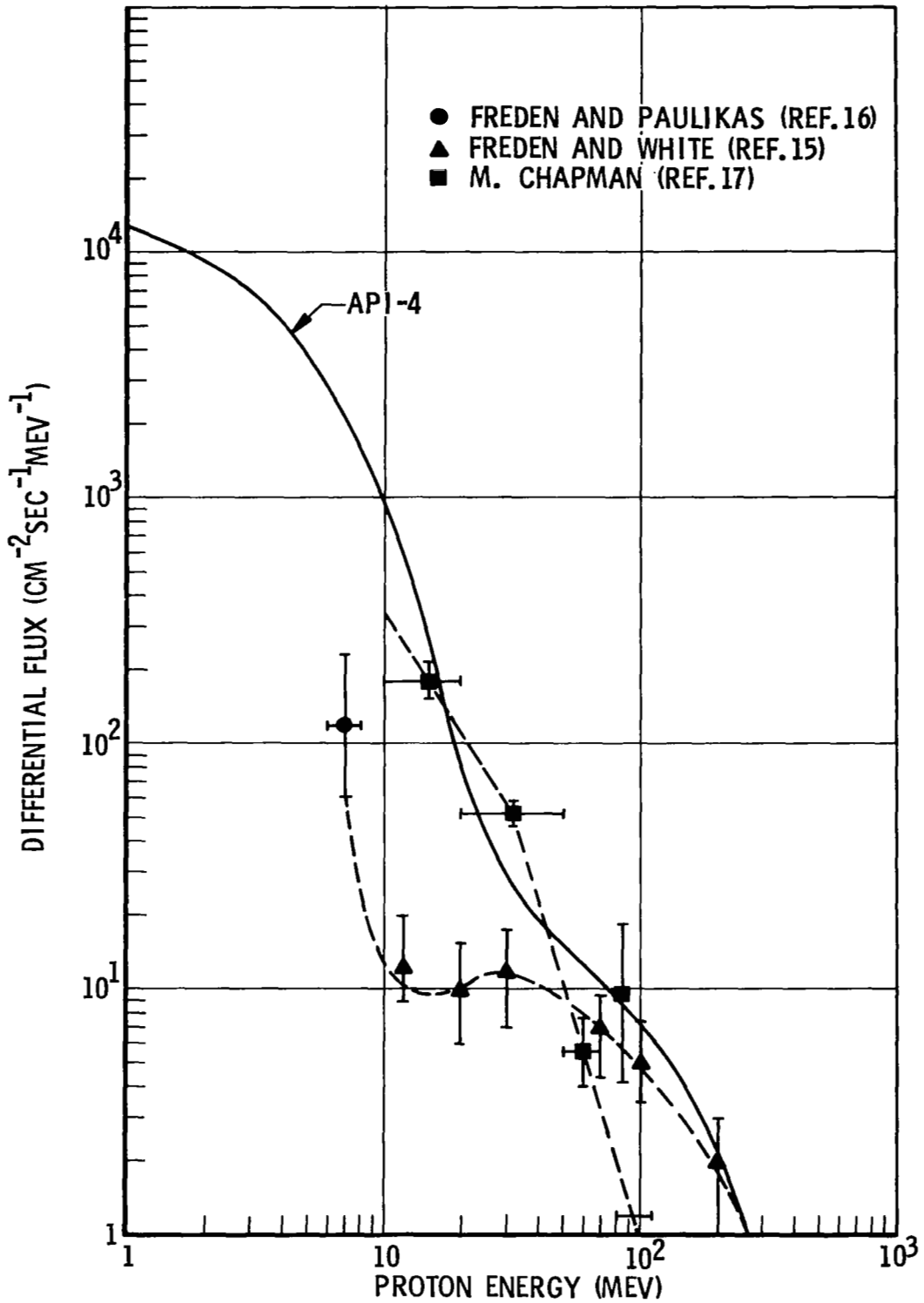
FIGURE 5: DIFFERENTIAL PROTON SPECTRUM AT B = 0.2 GAUSS
L = 1.3 EARTH RADII
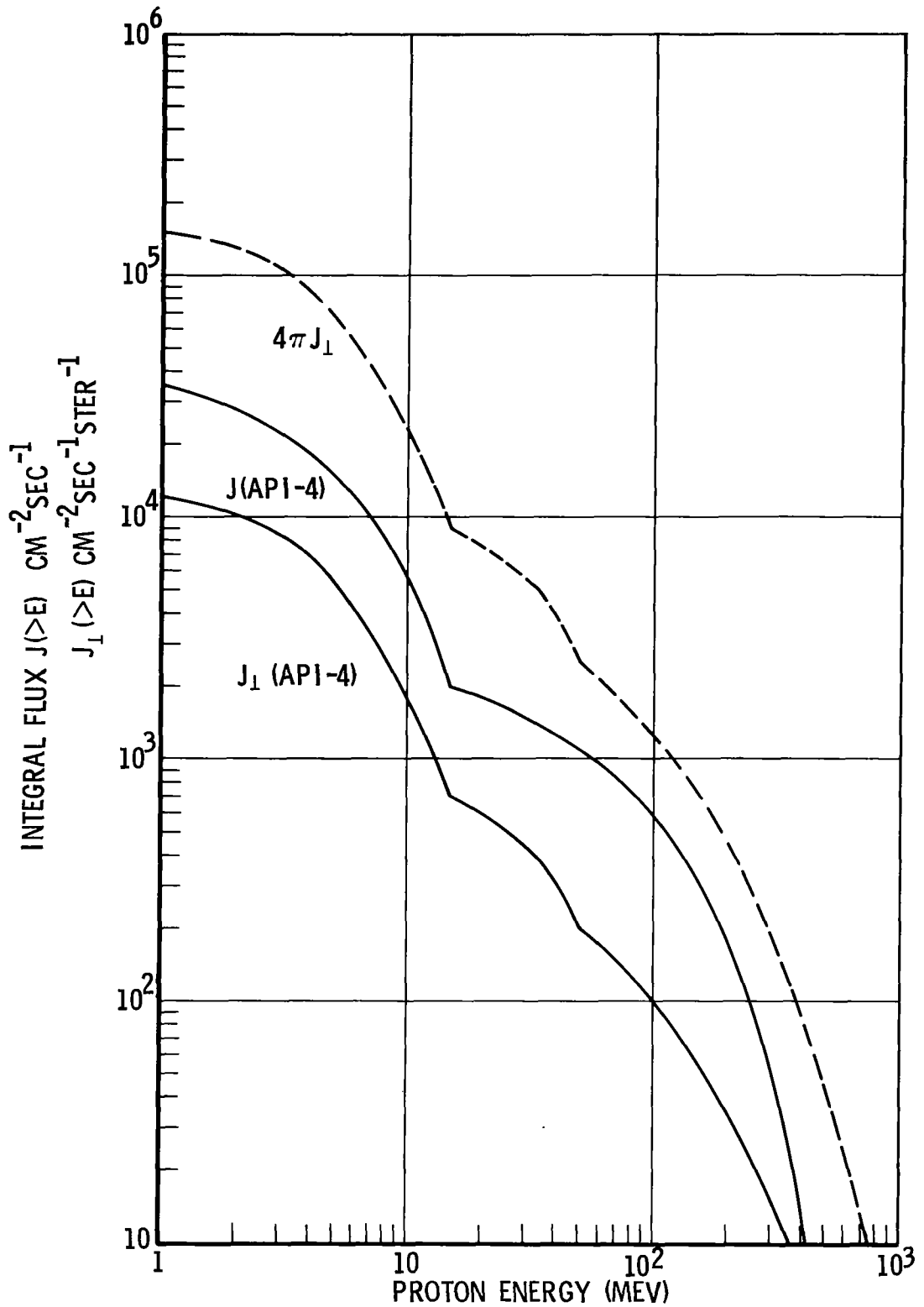
FIGURE 6: COMPARISON OF OMNIDIRECTIONAL AND UNIDIRECTIONAL
INTEGRAL SPECTRA , B = 0.2 GAUSS , L = 1.3 EARTH RADII
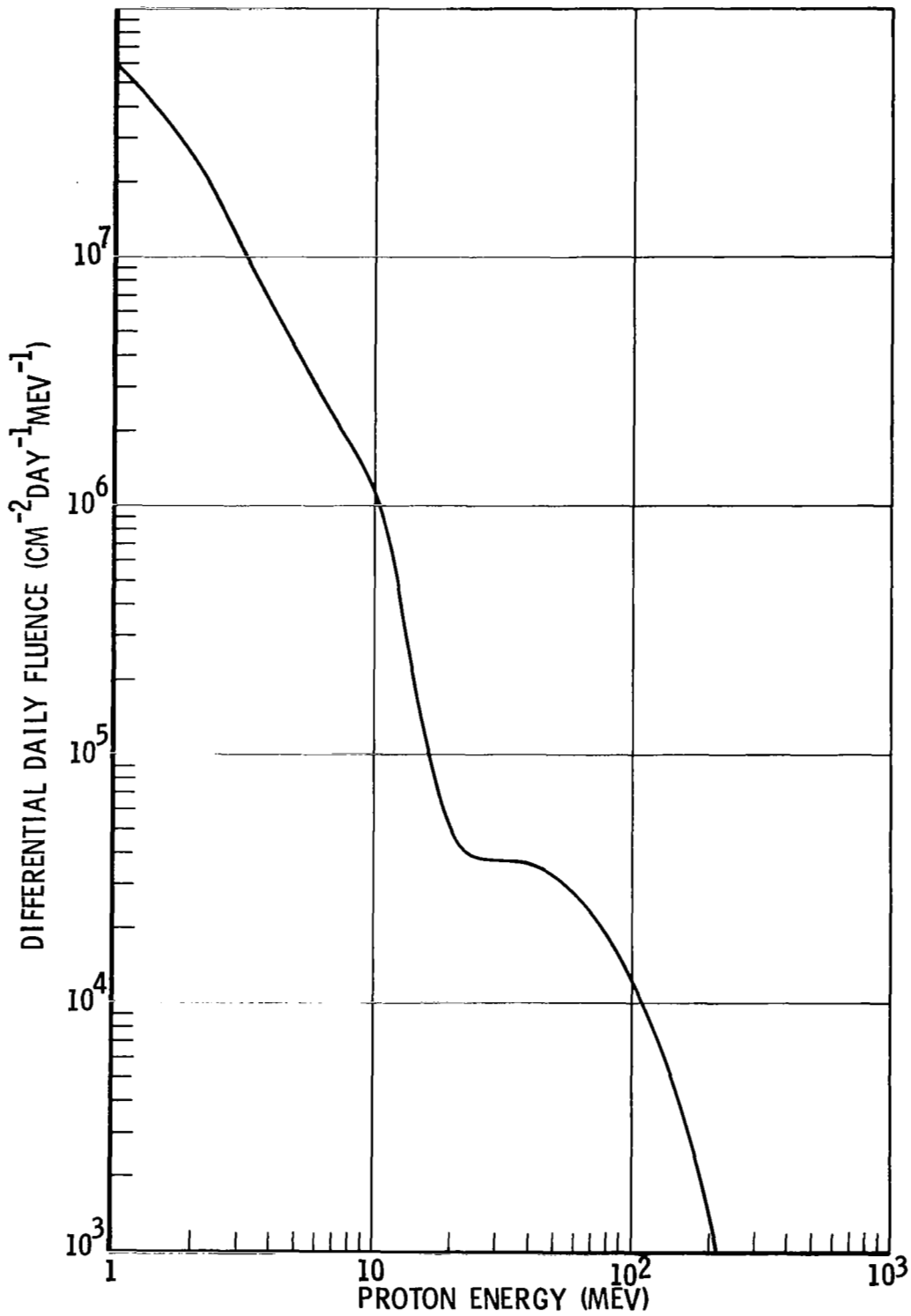
FIGURE 7: DAILY FLUENCE SPECTRUM OF TRAPPED PROTONS IN LOW
ALTITUDE ORBIT, 260 N.M. ALTITUDE, 50° INCLINATION
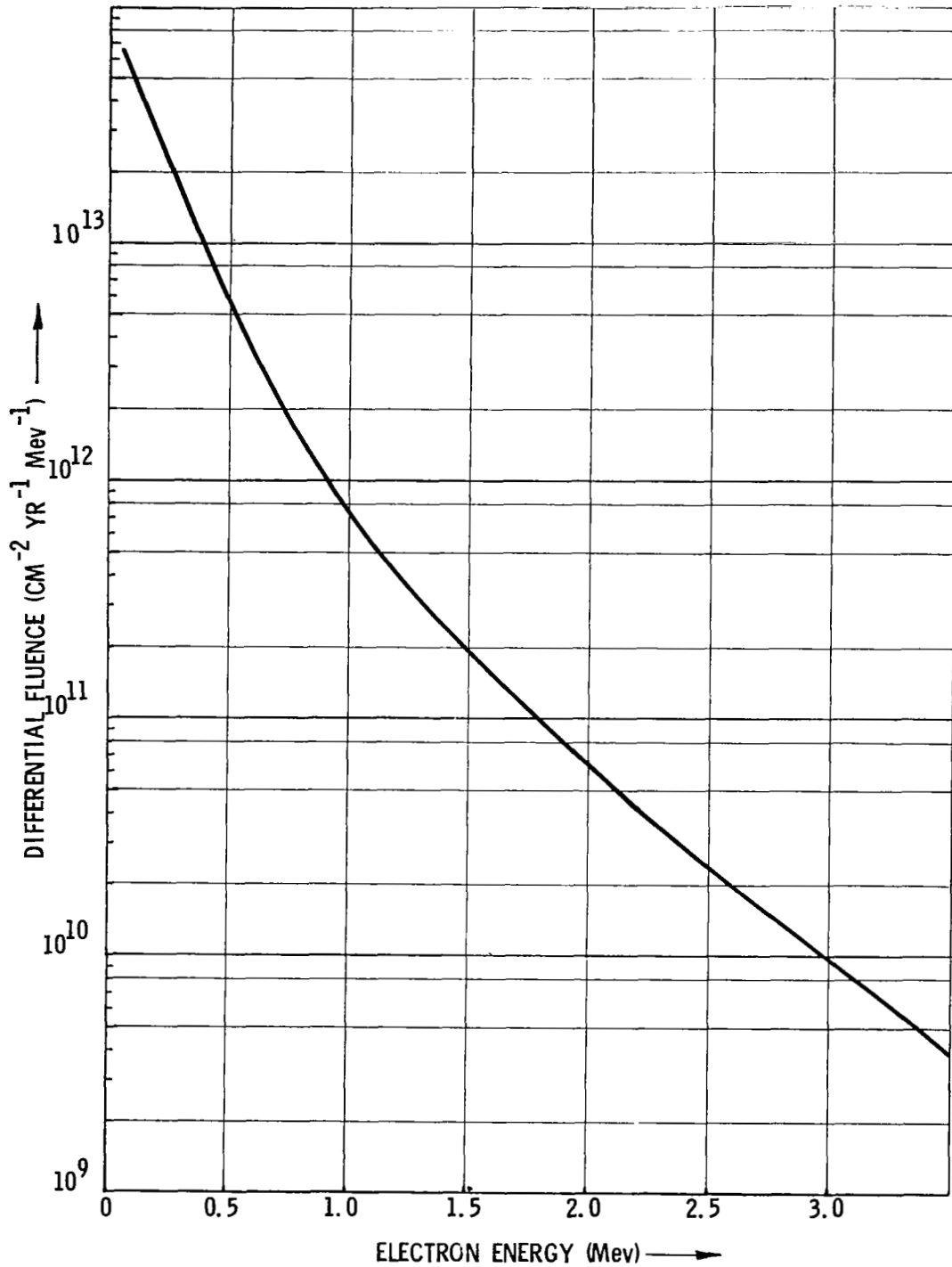
FIGURE 8

YEARLY FLUENCE SPECTRUM OF ELECTRON S IN LOW
ALTITUDE ORBIT: 260 N.M. ALTITUDE, 50^0 INCLINATION
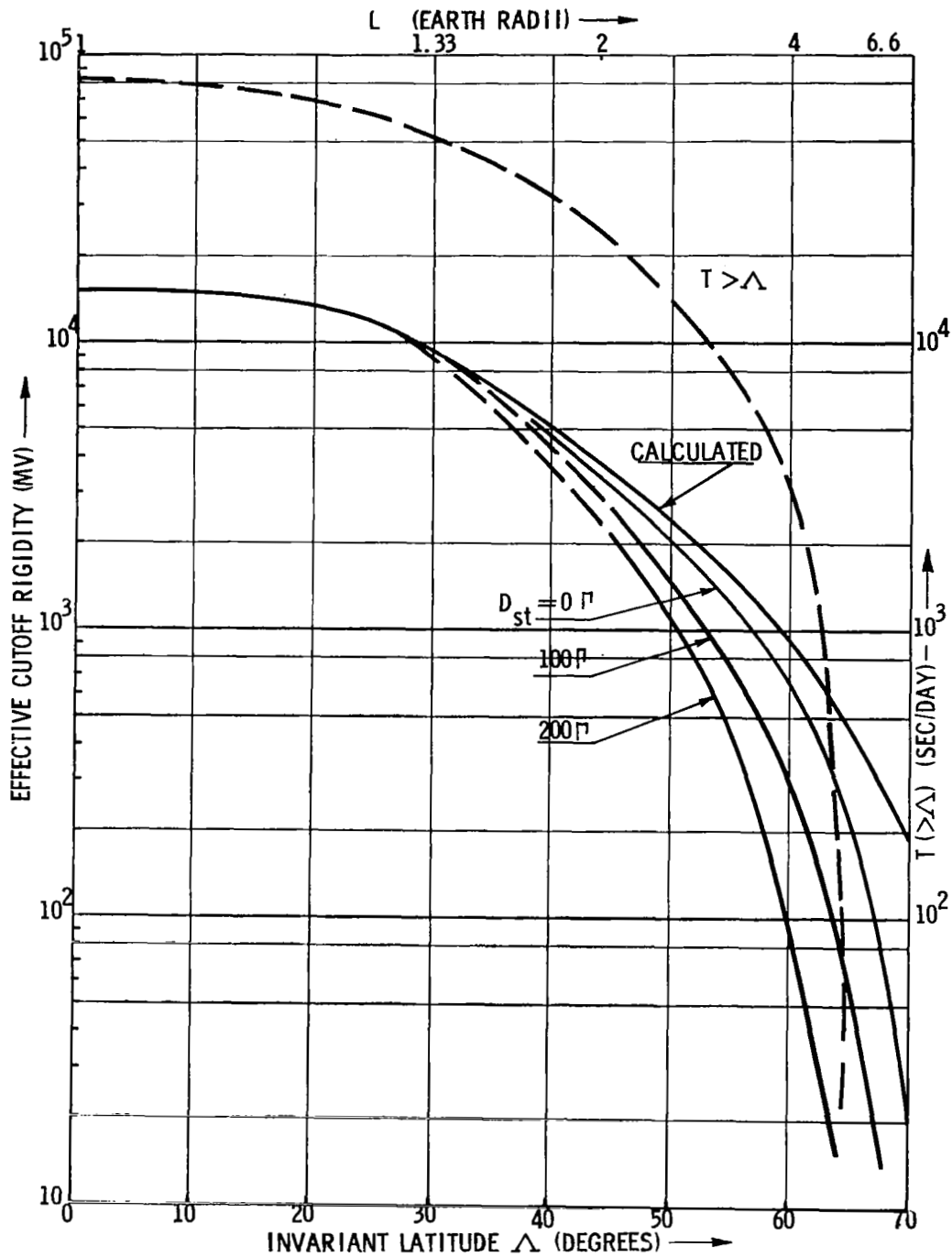
FIGURE 9

EFFECTIVE CUTOFF RIGIDITIES AND INTEGRAL TIME OF
ENCOUNTER FOR A LOW ALTITUDE 50° INCLINATION ORBIT
·260 N. M. ALTITUDE

41
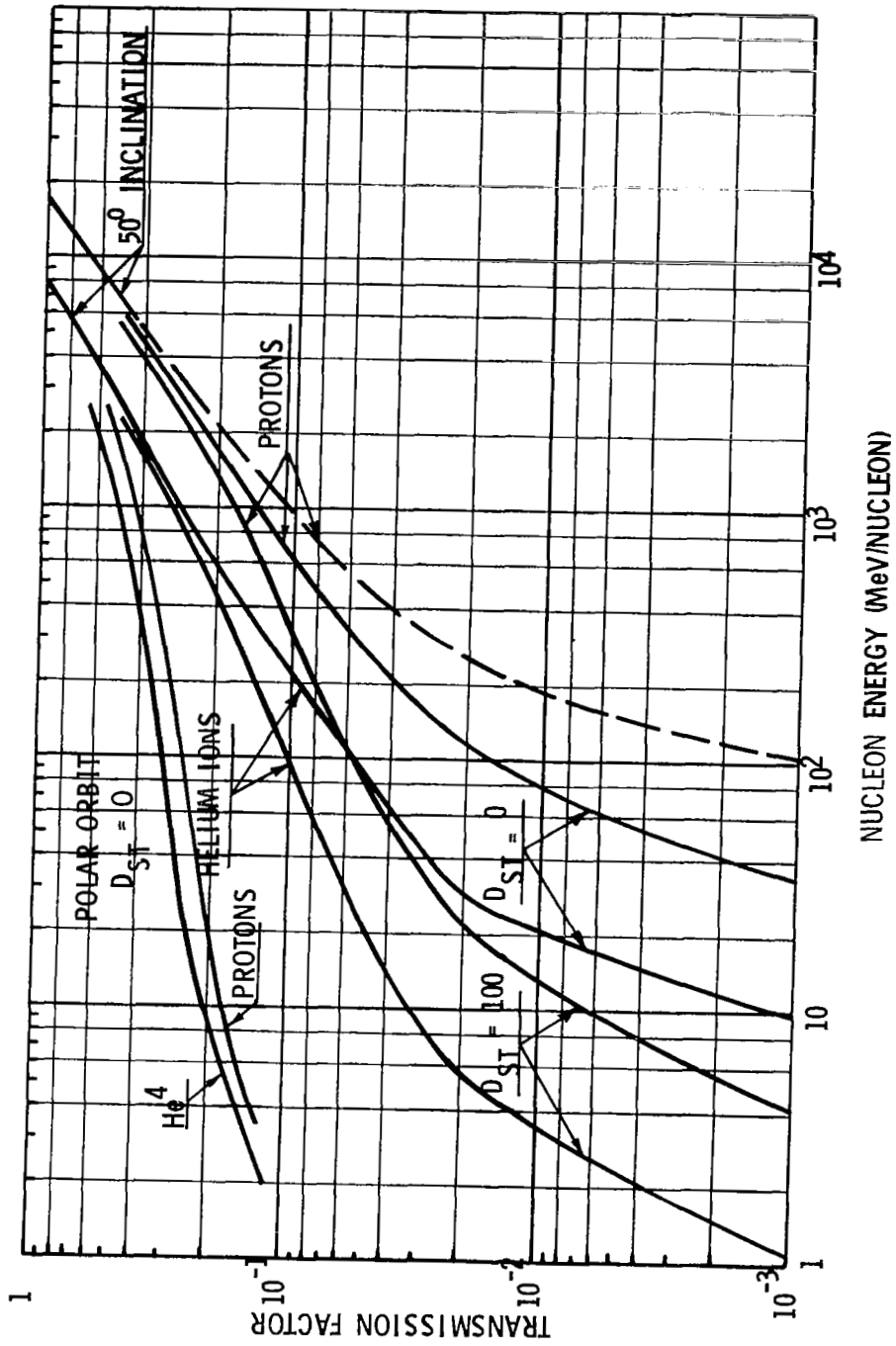
FIGURE 10

GEOMAGNETIC TRANSMISSION FACTOR FOR SOLAR
PARTICLES AND GALACTIC COSMIC RAYS
•260 N. M. ALTITUDE

42
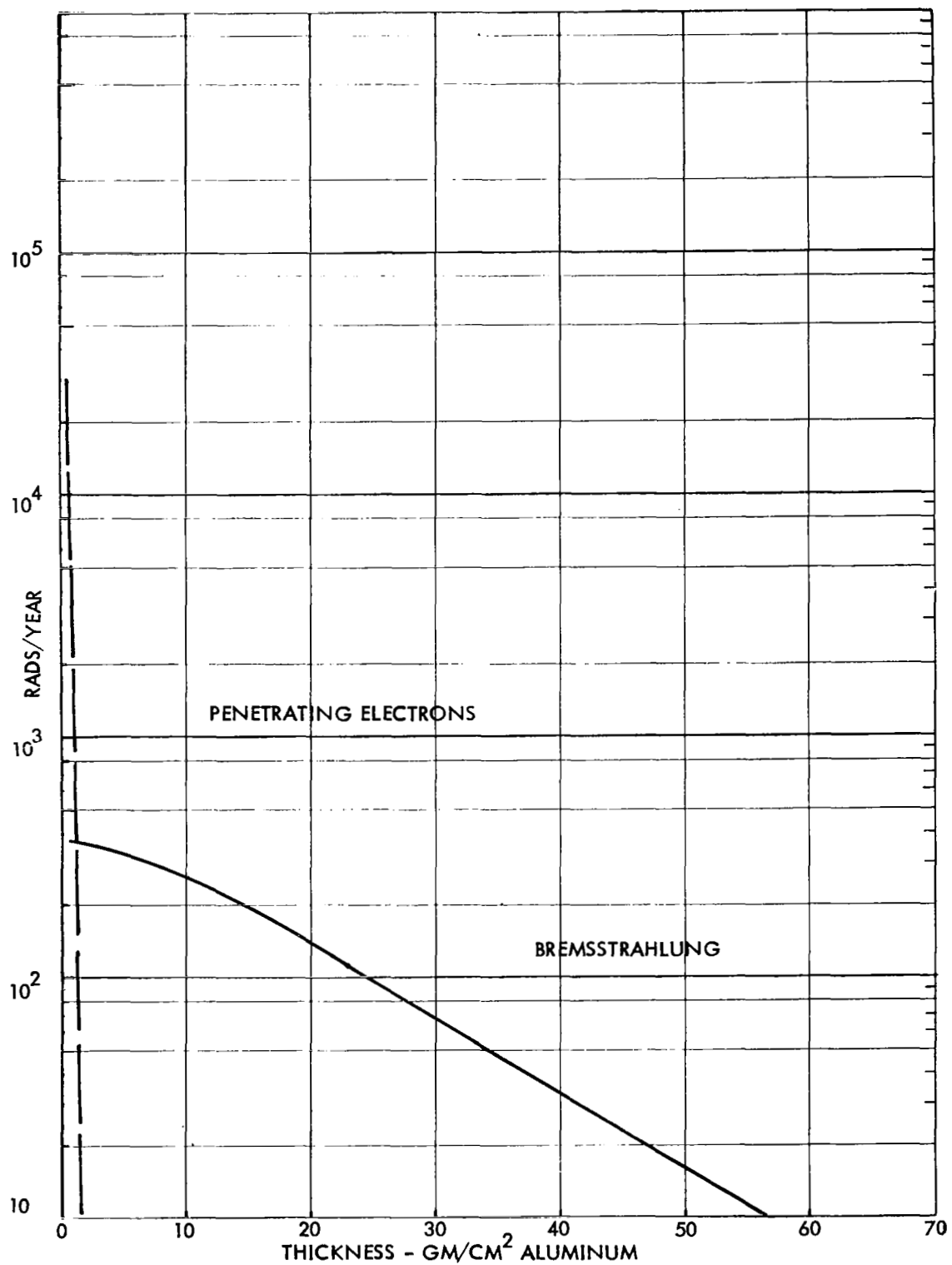
FIGURE 11
YEARLY DOSES FROM PENETRATING ELECTRONS AND BREMSSTRAHLUNG
AT SYNCHRONOUS ALTITUDE

43
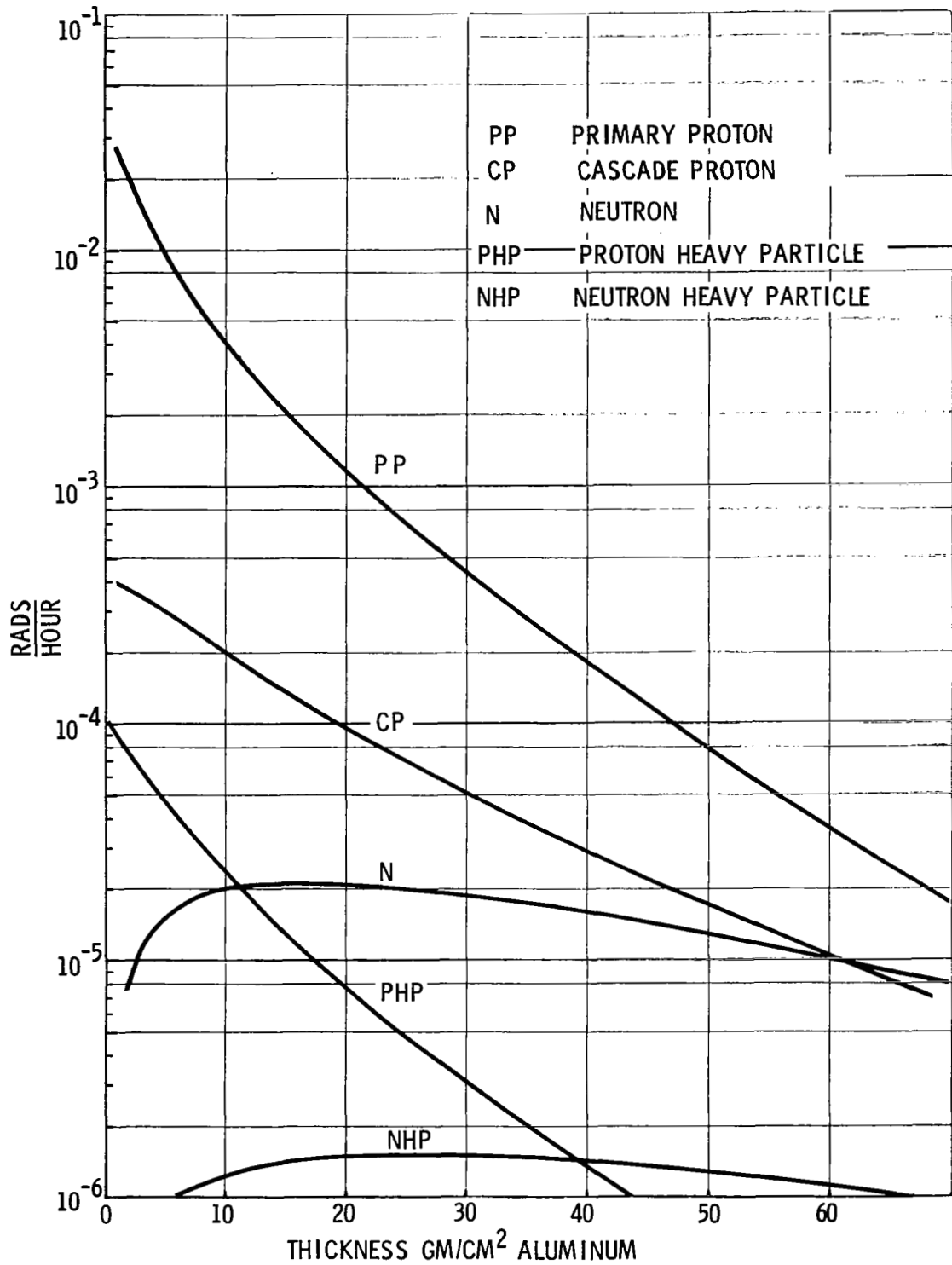
FIGURE 12   DEPTH-DOSE PROFILE FOR TRAPPED PROTONS
260 NAUTICAL MILE 50° INCLINATION CIRCULAR ORBIT
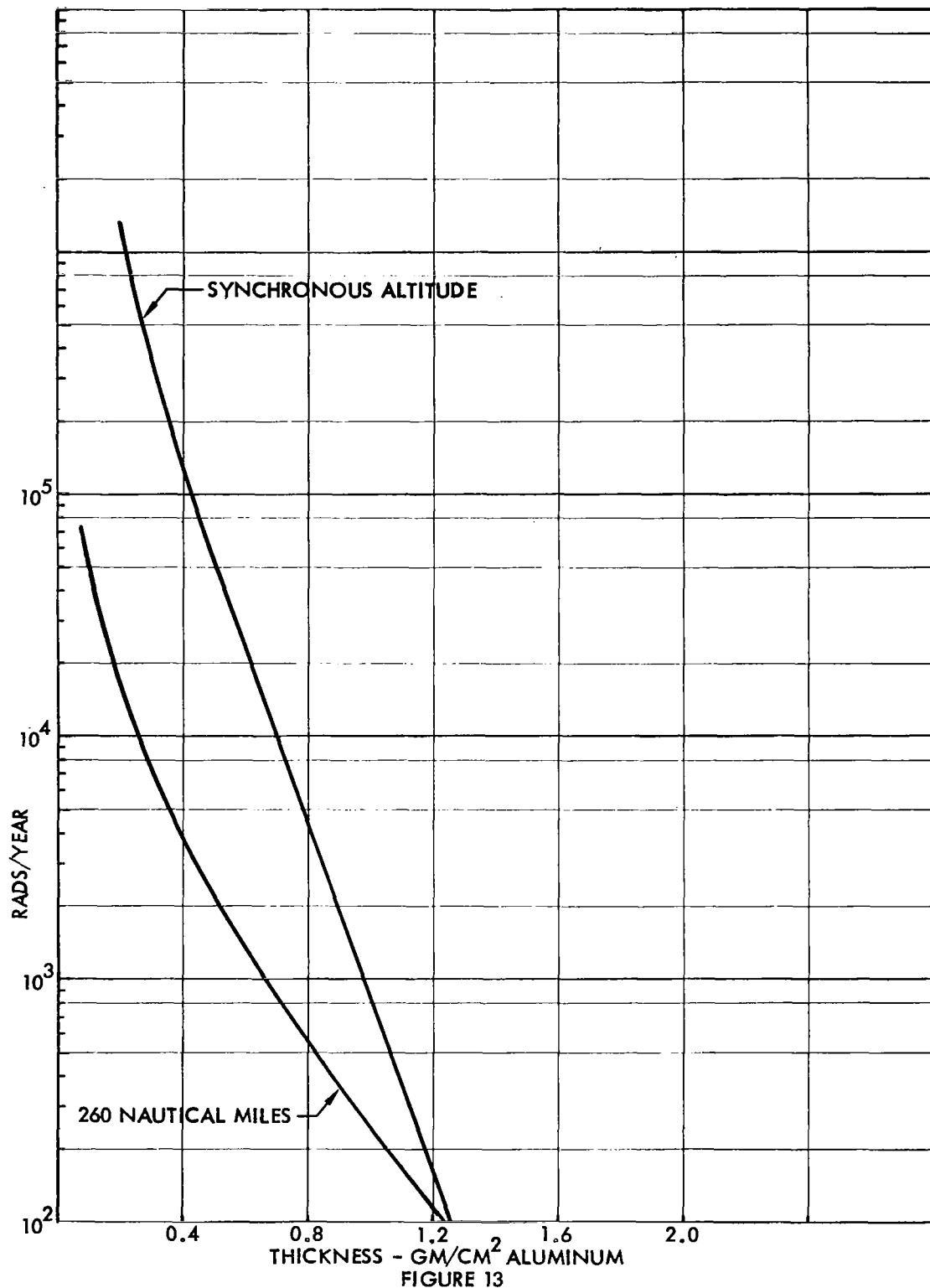
FIGURE 13

YEARLY DOSES FROM PENETRATING ELECTRONS AT SYNCHRONOUS AND 260 NAUTICAL MILES
50° INCLINATION ORBIT

45
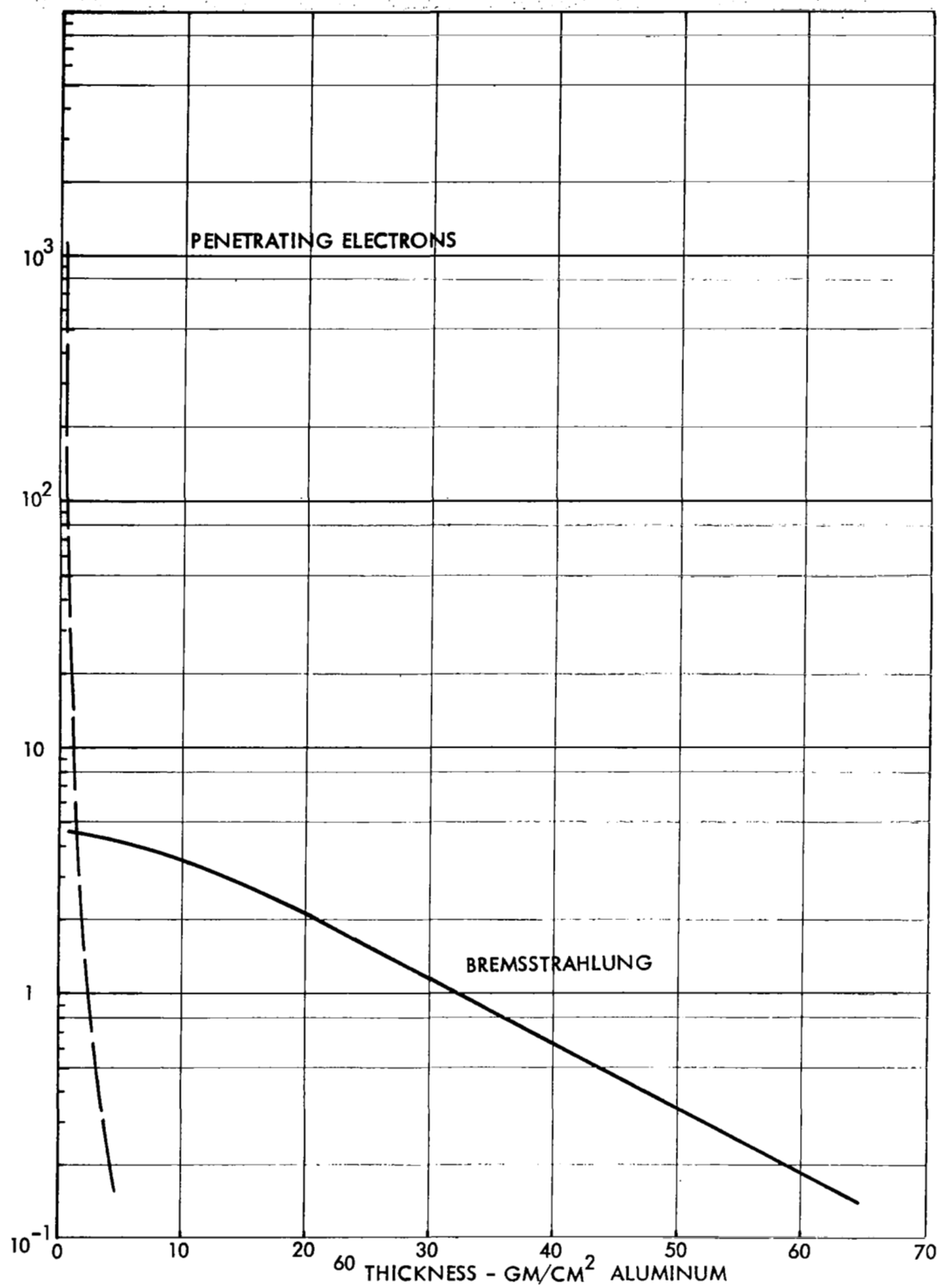
FIGURE 14
YEARLY DOSES FROM PENETRATING ELECTRONS AND BREMSSTRAHLUNG AT
NAUTICAL MILES, 50° INCLINATION ORBIT
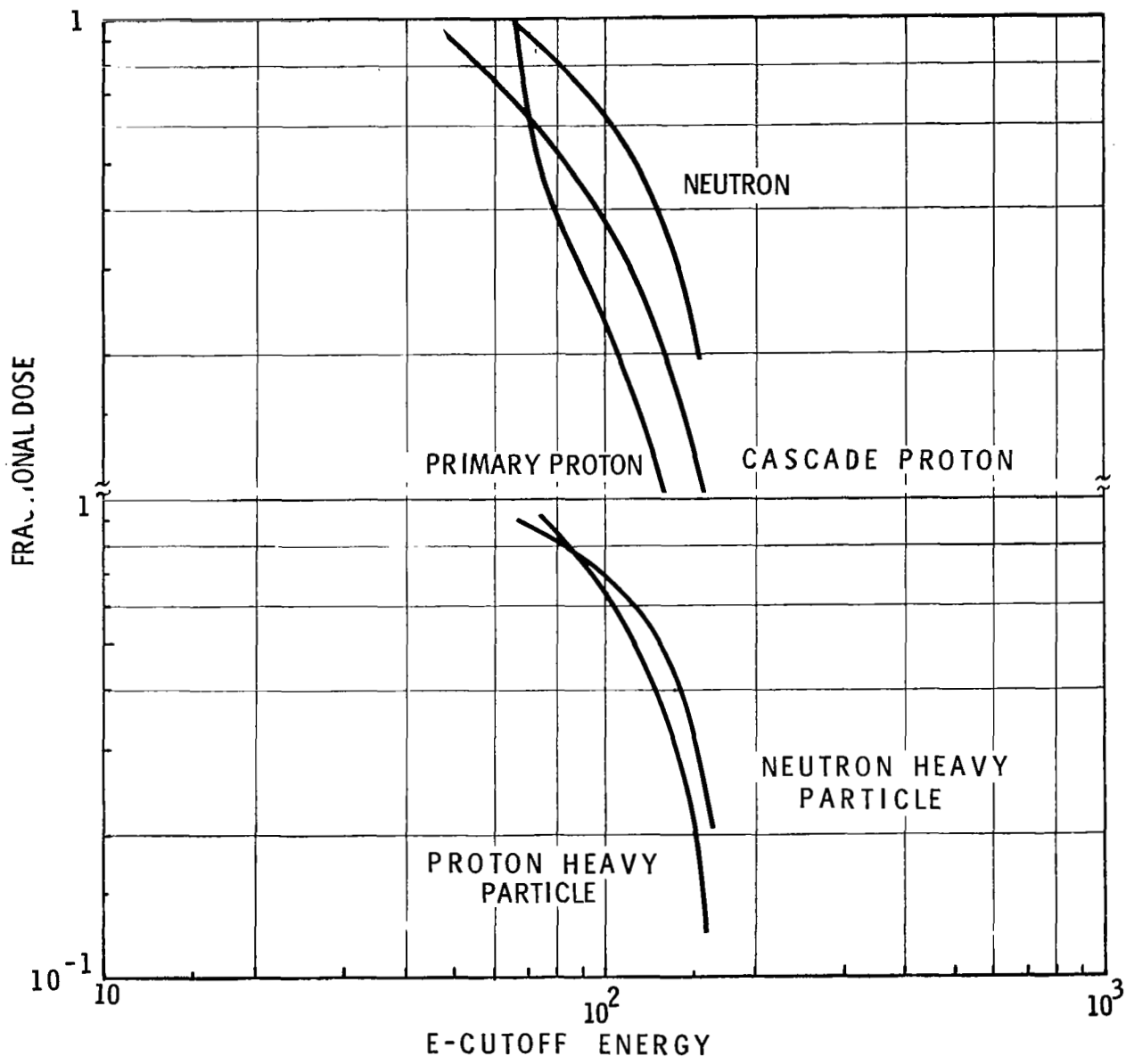
FIGURE 15: FRACTION OF DOSE FROM INCIDENT PROTONS OF ENERGY
$> E$ 260 NAUTICAL MILES, PROTONS INCIDENT ON
5 GM/CM^2 OF ALUMINUM
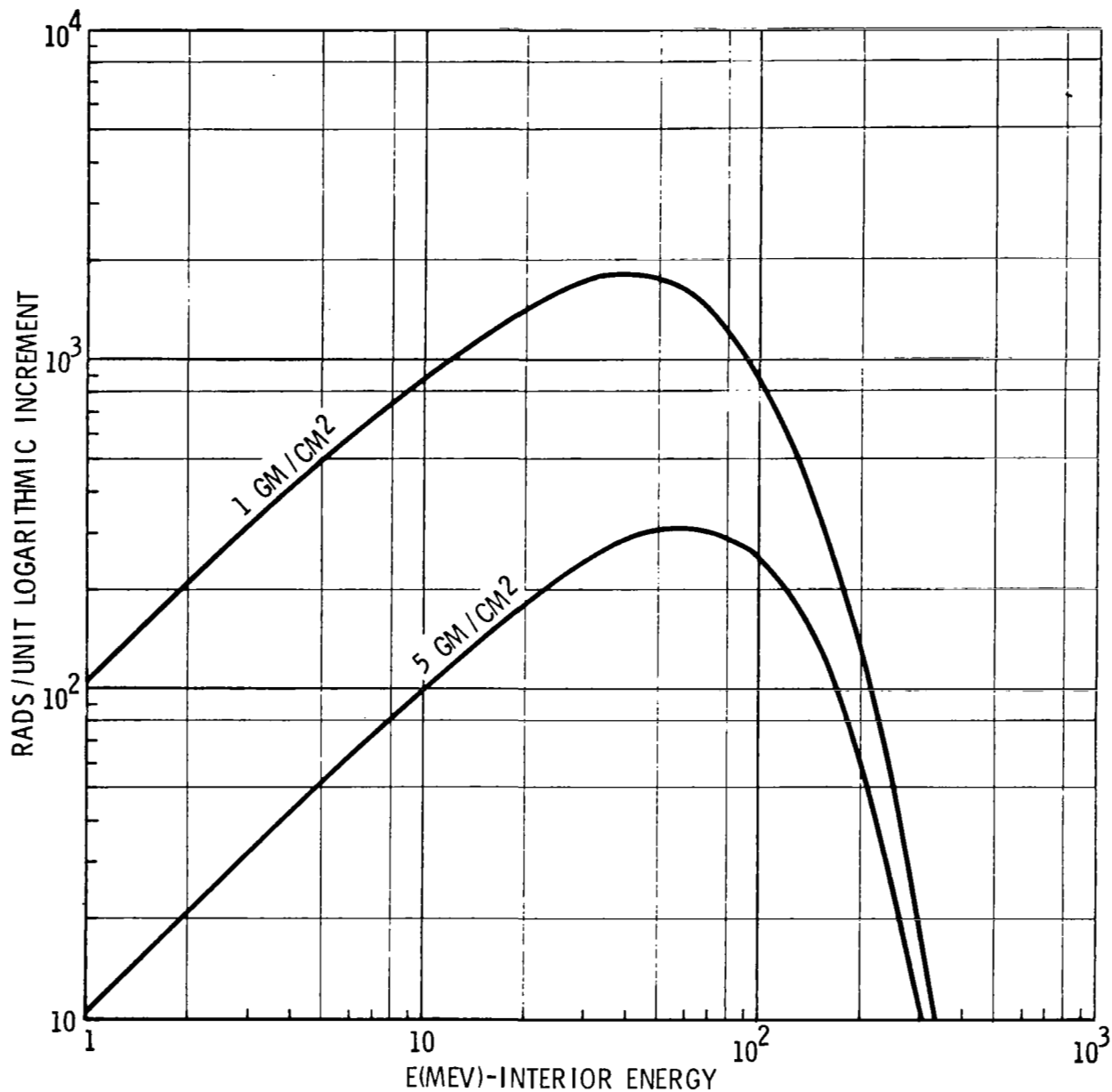
FIGURE 16: DIFFERENTIAL DOSE DISTRIBUTION FOR 260 NAUTICAL MILE
PROTON SPECTRUM INCIDENT ON ALUMINUM
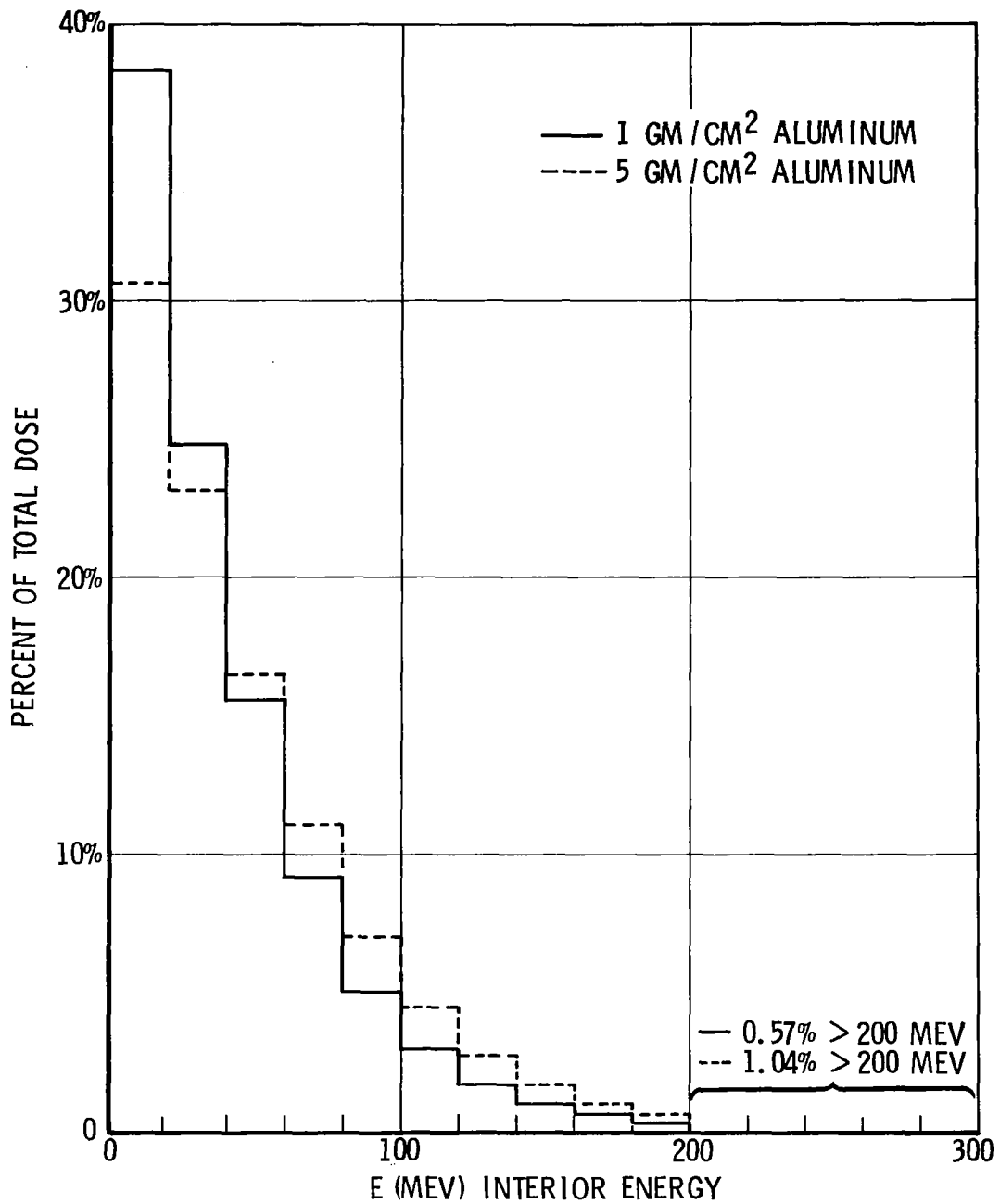
FIGURE 17: PERCENT DOSE RECEIVED IN 20 MEV ENERGY BANDS
260 NAUTICAL MILE PROTON SPECTRUM
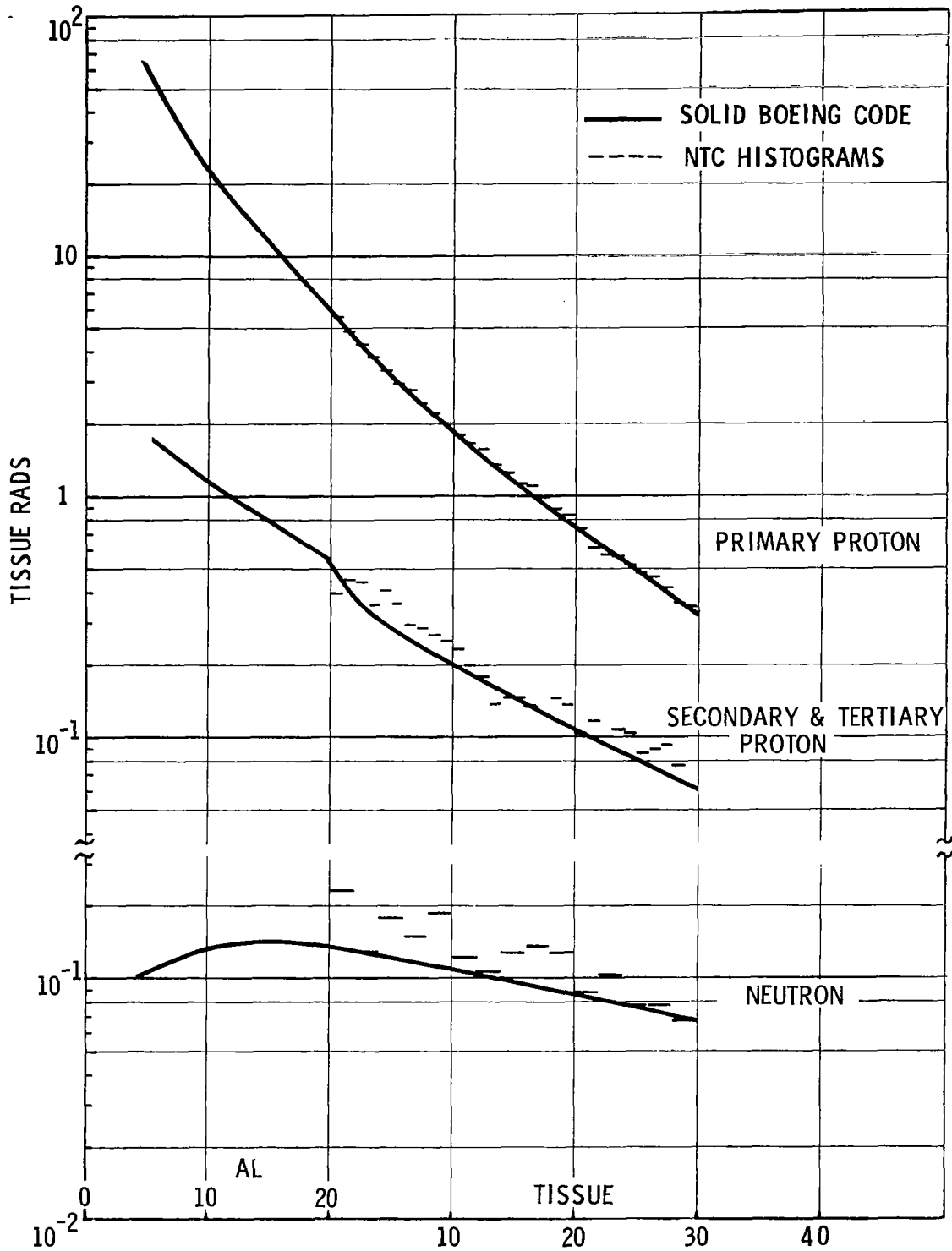
FIGURE 18: COMPARISON OF BOEING SECONDARY & OAK RIDGE NTC
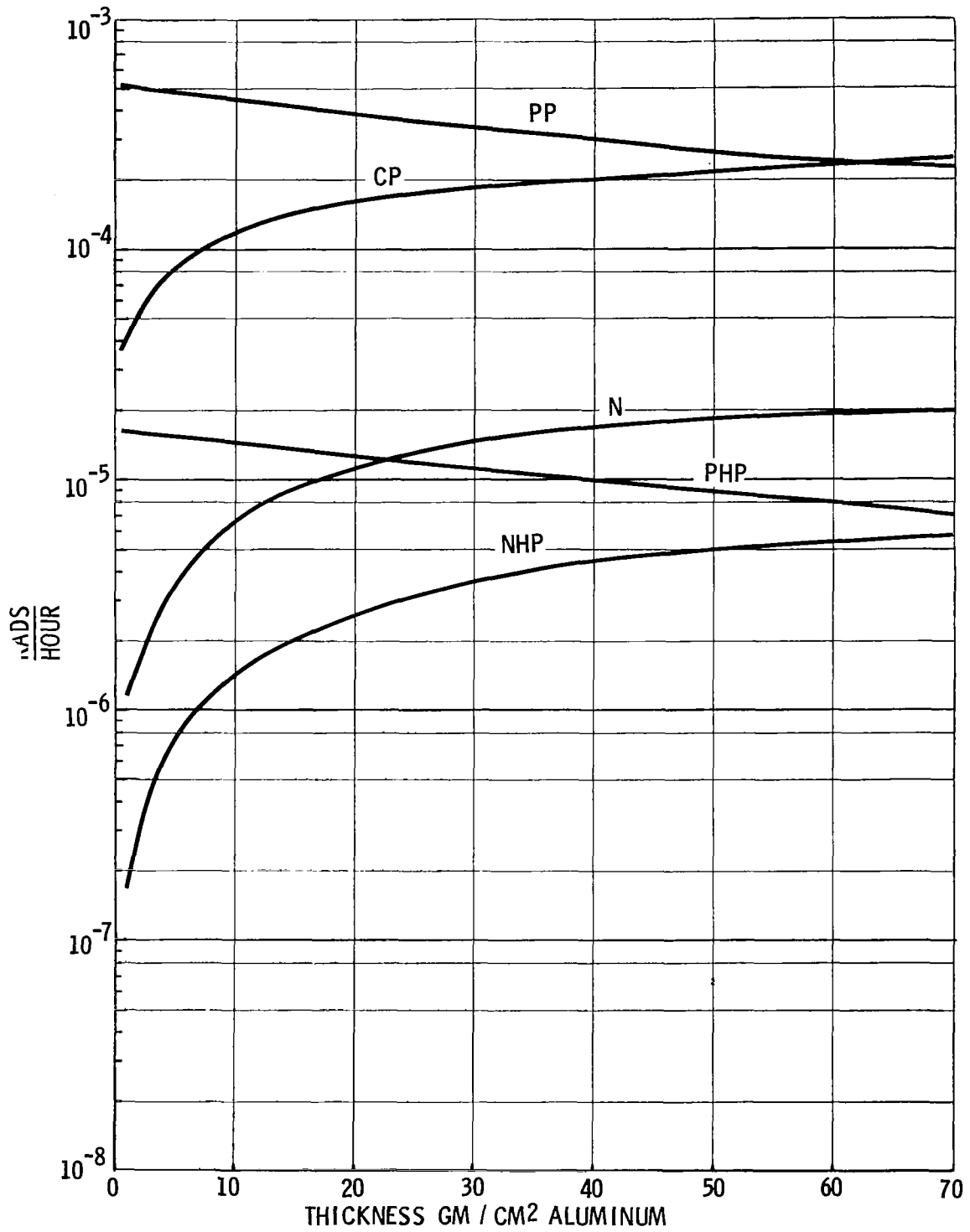
FIGURE 19: DEPTH-DOSE PROFILE FOR SOLAR MINIMUM GALACTIC
COSMIC-RAY PROTONS NORMALLY INCIDENT
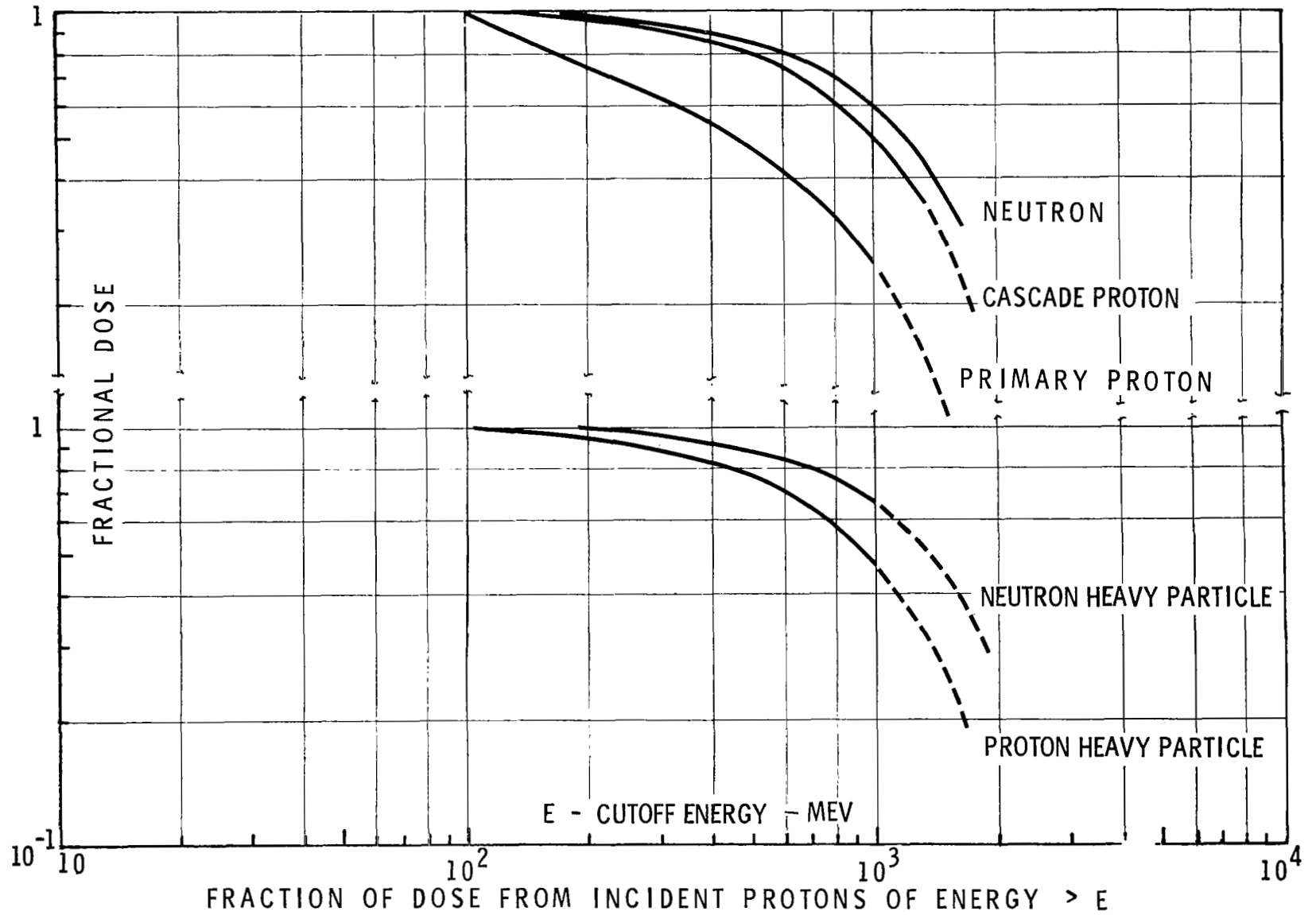
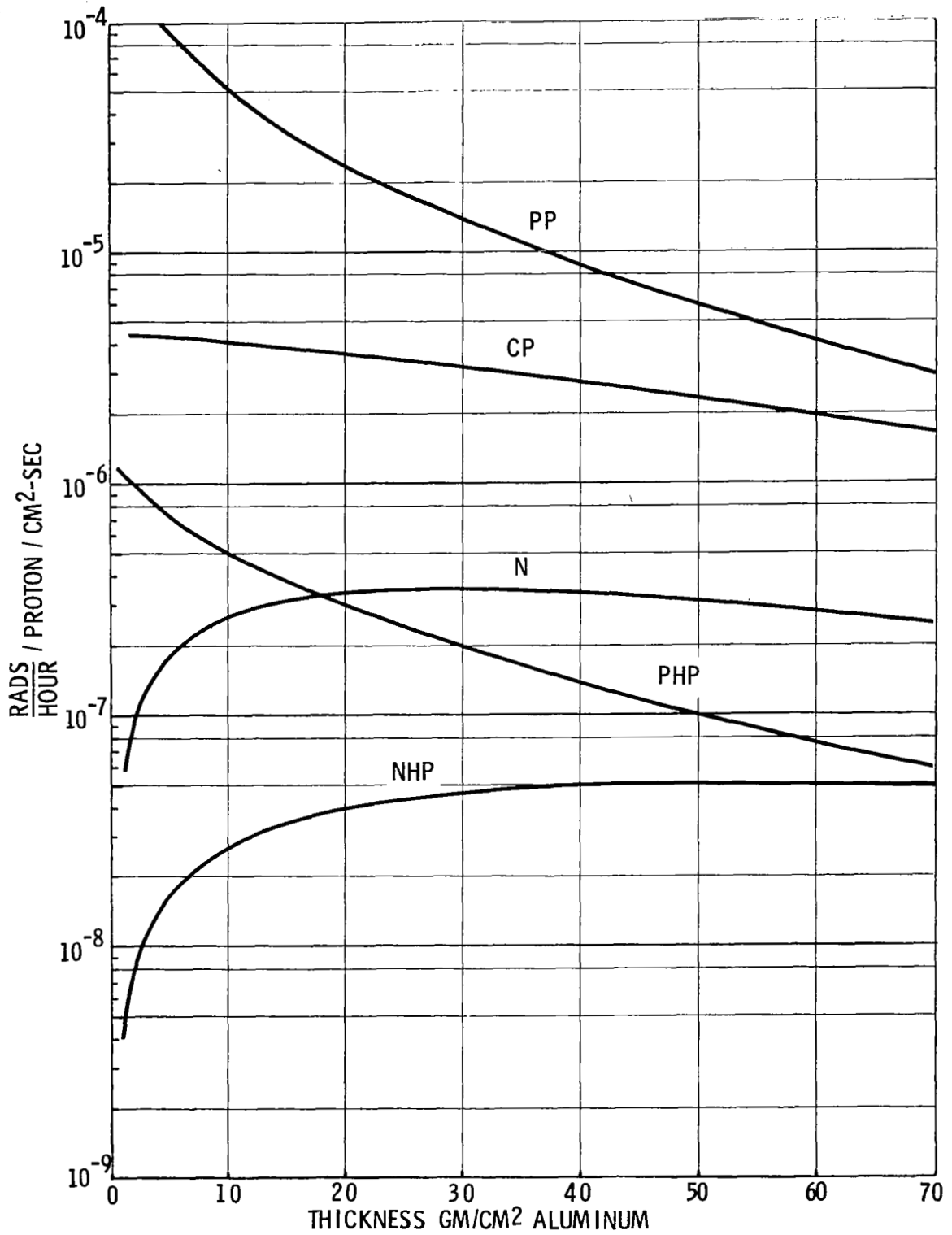FIGURE 20: GALACTIC PROTONS INCIDENT ON 10 GM/CM² OF ALUMINUM
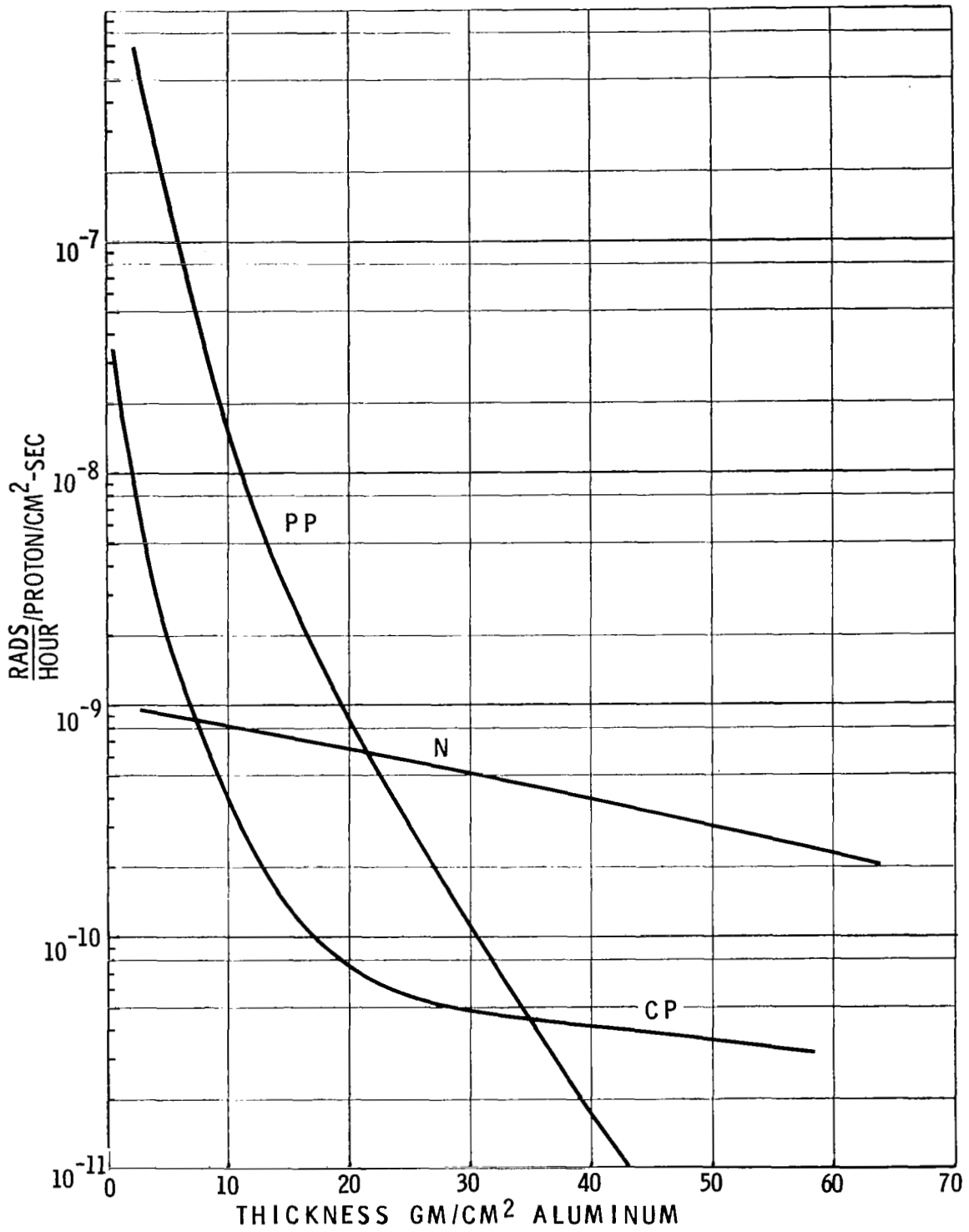
FIGURE 21: DEPTH-DOSE PROFILE FOR EXPONENTIAL RIGIDITY, SOLAR
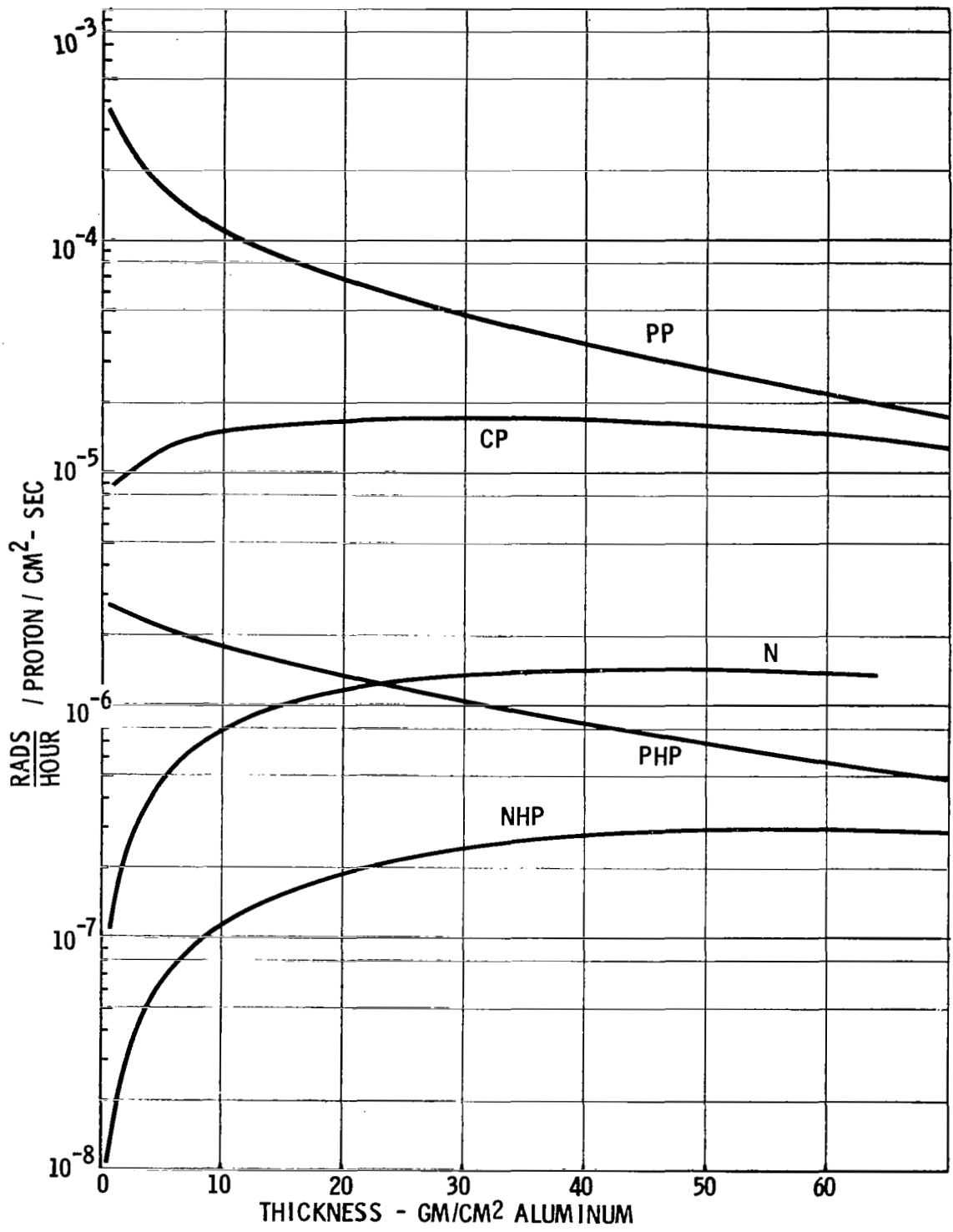PROTON SPECTRUM NORMALLY INCIDENT P_D = 40 MV
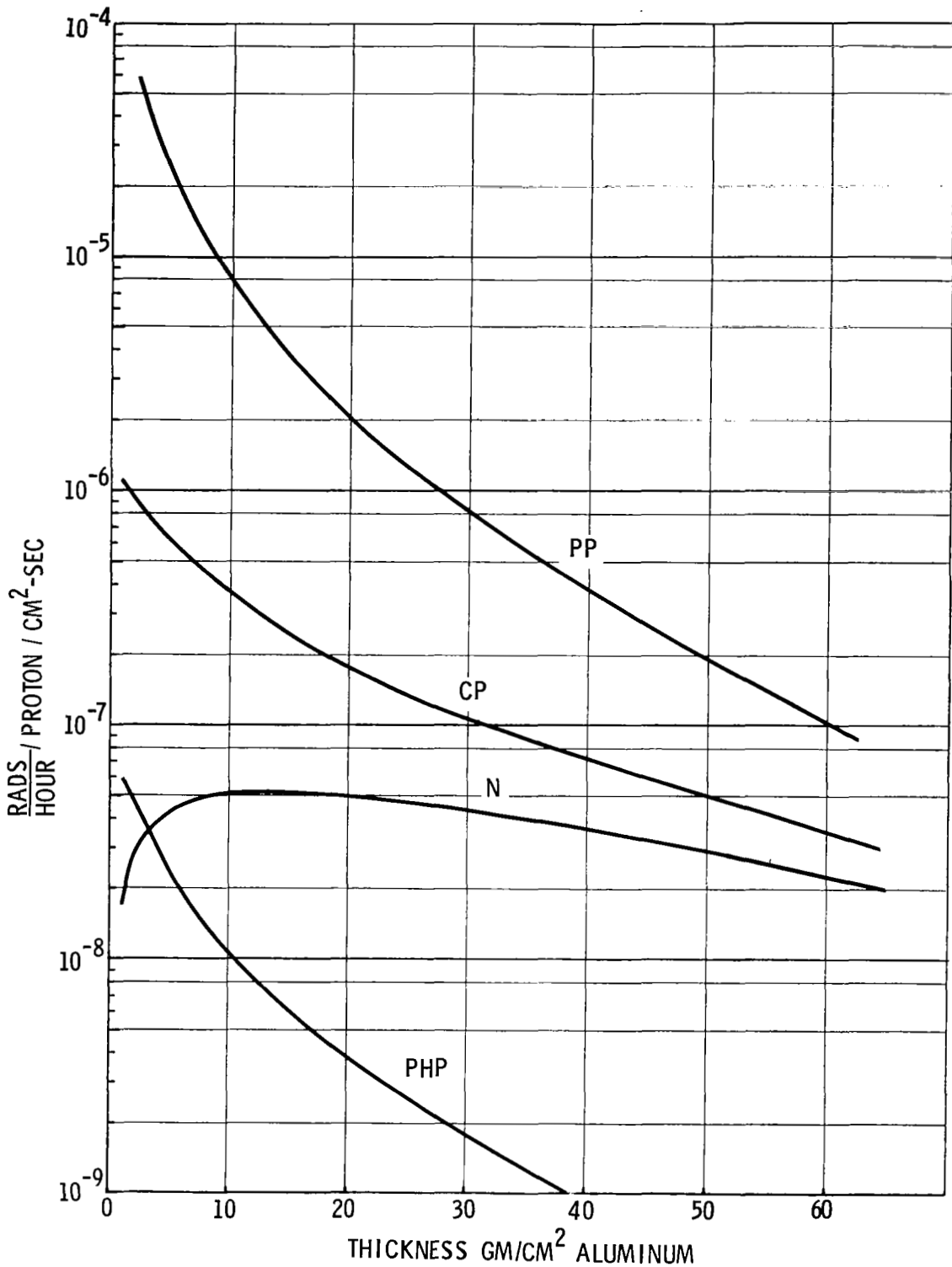
FIGURE 22: DEPTH-DOSE PROFILE FOR EXPONENTIAL RIGIDITY, SOLAR
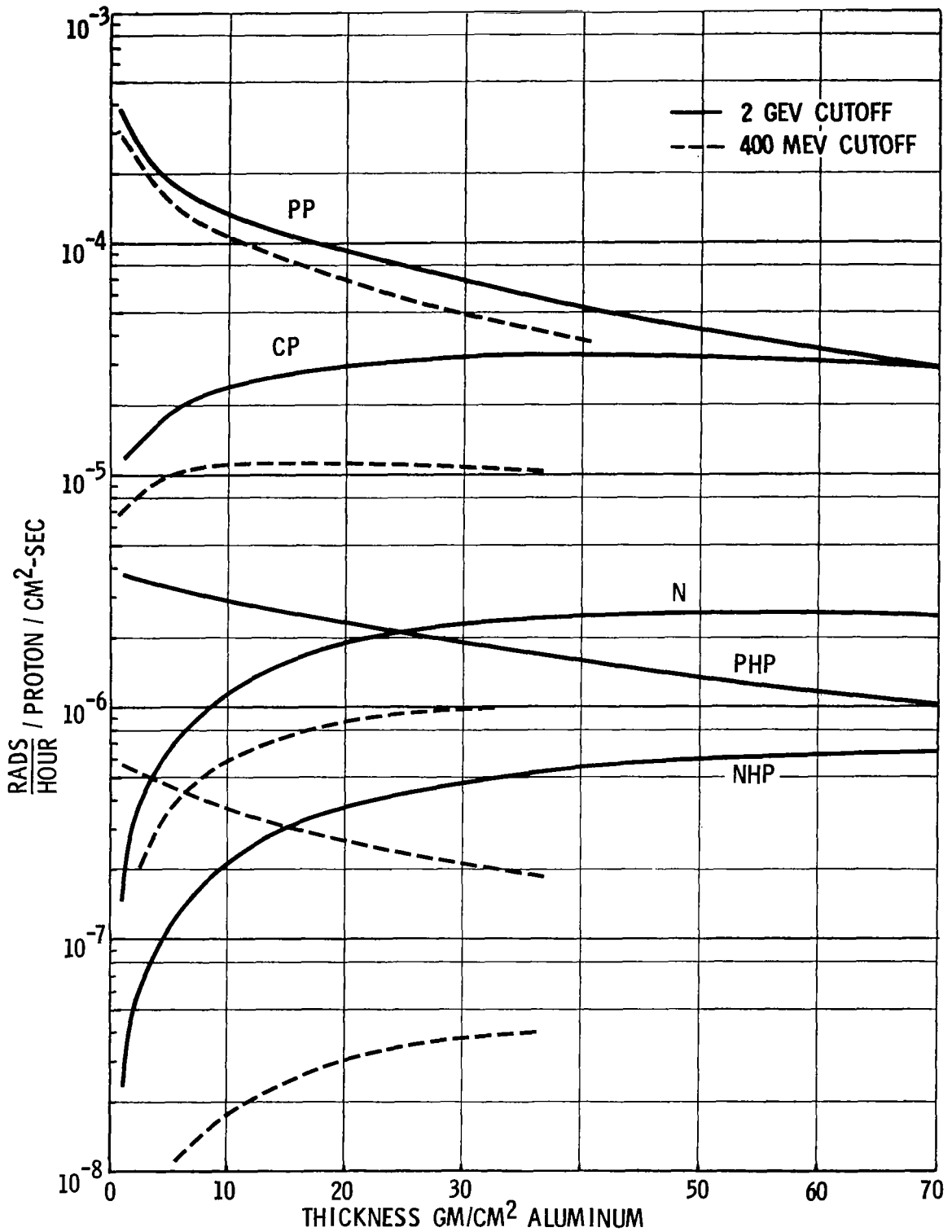PROTON SPECTRUM NORMALLY INCIDENT P_0 = 100 MV
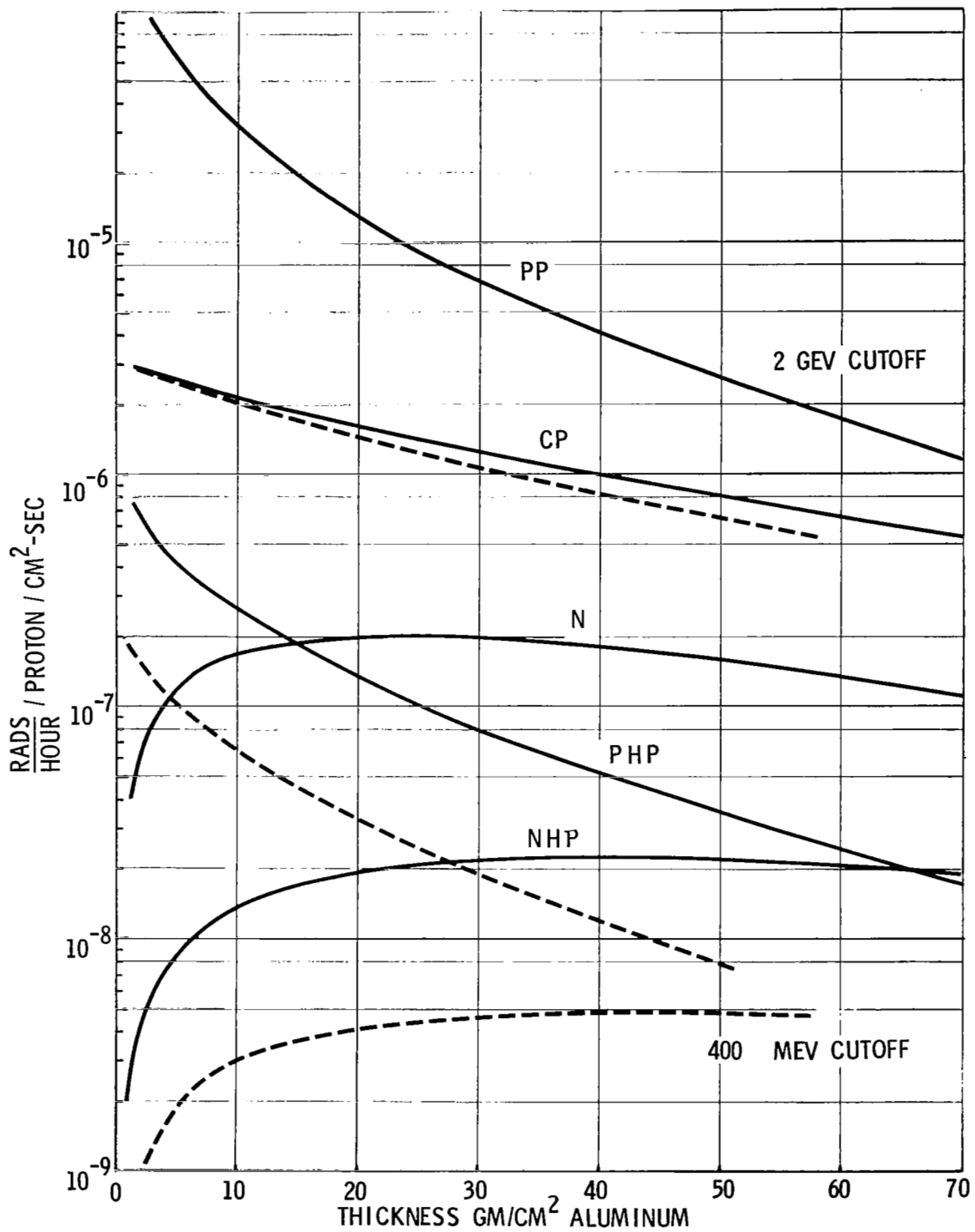
FIGURE 23: DEPTH-DOSE PROFILE FOR EXPONENTIAL RIGIDITY, SOLAR
PROTON SPECTRUM NORMALLY INCIDENT P_o = 160MV

FIGURE 24: DEPTH-DOSE PROFILE FOR EXPONENTIAL RIGIDITY, SOLAR
PROTON SPECTRUM NORMALLY INCIDENT P_0 = 200 MV

FIGURE 25: DEPTH-DOSE PROFILE FOR EXPONENTIAL RIGIDITY, SOLAR PROTON SPECTRUM NORMALLY INCIDENT P_0 = 400 MV

57

FIGURE 26: DEPTH-DOSE PROFILE FOR EXPONENTIAL RIGIDITY, SOLAR
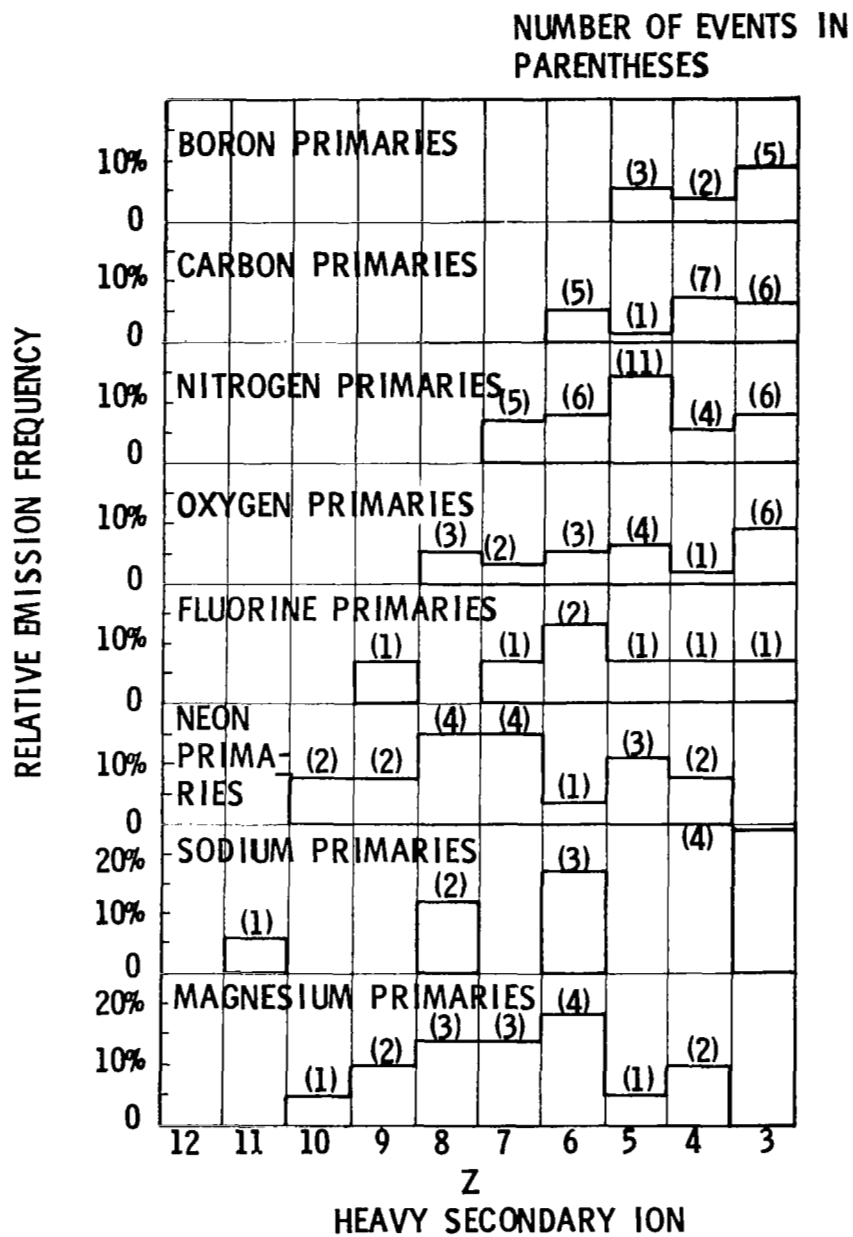PROTON SPECTRUM NORMALLY INCIDENT P_0 = 600 MV

FIGURE 27: RELATIVE EMISSION FREQUENCIES FOR HEAVY COSMIC
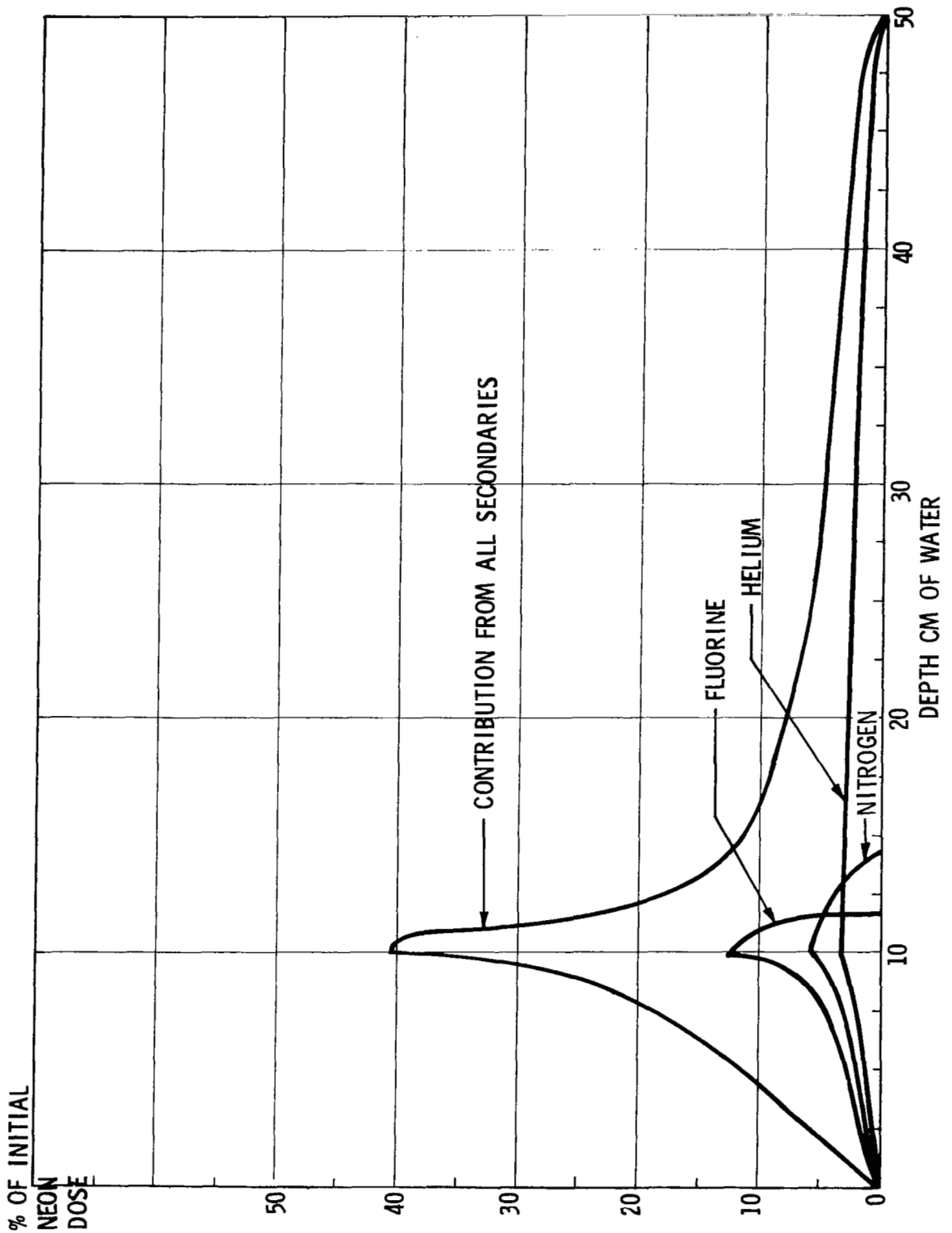RAY SECONDARIES

FIGURE 28: CONTRIBUTION TO THE BRAGG CURVE FROM SECONDARIES
300 MeV/NUCLEON NEON IONS IN WATER